# HOKKAIDO UNIVERSITY

Instructions for use

# Intercalation on transition metal trichalcogenides via a quasi-amorphous phase with 1D order

*Masaya Fujioka\*, Melbert Jeem, Kento Sato, Masashi Tanaka, Kazuki Morita Taizo Shibuya, Kiyonori Takahashi, Suguru Iwasaki, Akira Miura, Masanori Nagao, Satoshi Demura, Hideaki Sakata, Madoka Ono, Hideo Kaiju, and Junji Nishii1*

M. Fujioka, K. Sato, K. Takahashi, S.  Iwasaki, M. Ono, and J. Nishii
Research Institute for Electronic Science, Hokkaido University, Sapporo, Hokkaido 001-0020, Japan
E-mail: fujioka@es.hokudai.ac.jp

M. Jeem, A. Miura
Faculty of Engineering, Hokkaido University, Sapporo, Hokkaido 060-8628, Japan

M. Tanaka
Graduate School of Engineering, Kyushu Institute of Technology, 1-1 Sensui-cho, Tobata, Kitakyushu 804-8550, Japan

K. Morita
Department of Chemistry, University of Pennsylvania, Philadelphia, Pennsylvania 19104-6323, USA

T. Shibuya
System Platform Research Laboratories, NEC Corporation, 1753 Shimonumabe, Nakahara, Kawasaki 211-8666, Japan

M. Nagao
Center for Crystal Science and Technology, University of Yamanashi, Kofu, Yamanashi 400-0021, Japan

S. Demura
College of Science and Technology, Nihon University, 1-8-14 Surugadai, Kanda, Chiyoda-ku, Tokyo 101–8308, Japan

H. Sakata
Department of Physics, Tokyo University of Science, 1-3 Kagurazaka Shinjyuku-ku Tokyo 162-8601, Japan.

H. Kaiju
Department of Applied Physics and Physico-Informatics, Faculty of Science and Technology, Keio University, Yokohama, Kanagawa 223-8522, Japan

**Abstract**

Intercalation into one-dimensional (1D) transition metal trichalcogenides (TMTs) in which fibers are bonded by a weak van der Waals force can be expected to create various intercalation compounds and develop unique physical properties according to the combination of the host materials and guest ions. However, structural changes via intercalation into 1D TMTs are not as simple as those in two-dimensional (2D) transition metal dichalcogenides (TMDs) and are still not understood comprehensively. $ZrTe_3$: a typical compound with a 1D trigonal prismatic structure, belongs to TMTs. Herein, through the Ag introduction to $ZrTe_3$ via solid-state intercalation, a novel crystal phase with a 1D octahedral structure and a quasi-amorphous phase during the structural transition have been discovered; the quasi-amorphous phase is a novel state of matter in which long-range order is lost while retaining 1D order. Based on the Ag concentration, the transport properties are flexibly modulated from superconductivity to semiconductivity. Density functional theory calculations indicate the attraction between Ag ions and the pair diffusion due to their attraction. Furthermore, judging the attraction or repulsion between guest ions would predict whether to induce a quasi-amorphous phase or simple lattice expansion like the intercalation into 2D TMDs.

## 1. Introduction

Transition metal trichalcogenides (TMTs) are expressed as $MX_3$, where M = Ti, Zr, Hf, etc., and X = S, Se, or Te. TMTs exhibit a one-dimensional (1D) trigonal prismatic unit and comprise six coordinated chalcogens centered on transition metals.[1] A van der Waals gap surrounds each 1D unit, which extends along the *b*-axis, and spreads in the crystal structure three-dimensionally. However, in the case of two-dimensional (2D) materials, such as graphite and transition metal dichalcogenides (TMDs), van der Waals gaps spread in 2D interlayer spaces. Therefore, more guest species can accumulate in TMTs than in TMDs. Three equivalents or more of Li ions have been introduced into TMTs,[2] though TMDs can generally accommodate only approximately one equivalent.[3] Owing to such a high ion accommodation capacity, TMTs have attracted attention as electrode materials for ion batteries.[4] Furthermore, because the ion concentration can be adjusted over a wide range, the electronic characteristics of TMTs should be modulated flexibly based on the guest ion concentration. Thus, TMTs, which show a higher guest-ion accommodation capacity than TMDs, are expected to afford more excellent functionality.

However, unlike the 2D layered compounds, structural changes in TMT intercalation compounds cannot be comprehended by the simple expansion of the lattice constant.[5] Structural analysis is the most challenging issue in treating the TMT intercalation compounds because the intercalation into three-dimensionally spread van der Waals gaps induces flexible structural changes and reduces the crystallinity. Elucidating the crystal structure of TMT compounds after the intercalation process is one of the critical topics in this family.

Generally, although the mainstream approach for intercalation is a liquid-phase process, the decrease in the crystallinity of the compound owing to the simultaneous intercalation of the solvent further hinders structural analysis. Thus far, Li intercalated TMT has been well investigated via a liquid-phase process,[6] focusing on a high-capacity Li-ion battery; however,

it is challenging to promote intercalation into 1D materials while maintaining sufficient crystallinity to clarify the fractional coordinates of each element.

In this study, a proton-driven ion introduction (PDII)[7]: solid-state intercalation based on the anisotropic ion diffusion,[8] was employed to introduce Ag ions into $ZrTe_3$,[9] which is a member of the TMT families with a 1D structure. Ag was adopted as the guest ion because of its higher stability than alkali metal ions[7a] and diffusibility than Cu ions among monovalent cations. Fiber-like samples were prepared without structural decomposition via PDII. Figure S1 shows the detailed synthesis condition, and Figure 1(a) shows the optical image for an as-prepared sample.

## 2. Phase transition from trigonal prismatic to octahedral phases

$ZrTe_3$ intercalation compounds with diluted guest ions, such as $Ni_{0.05}ZrTe_3$,[10] $Fe_{0.05}ZrTe_3$,[11] $Cu_{0.05}ZrTe_3$,[10, 12] and $Ag_{0.05}ZrTe_3$,[12a] have been reported. However, no X-ray diffraction (XRD) peak shifts through intercalation have been confirmed among these materials. It has been considered that the no-peak shift was caused by the low guest ion concentration.[12a] However, this study demonstrated that even when the Ag ions were intercalated in $ZrTe_3$ (i.e., $Ag_xZrTe_3$) at up to x = 1.0, structural changes could not be observed via synchrotron XRD (SXRD) measurements.

**Figure 1(b)** shows one of the fibrous samples peeled off from the as-prepared sample. The elemental composition of each fiber was analyzed using scanning electron microscopy (SEM) and energy-dispersive X-ray spectroscopy (EDS) (**Figure S2**). Through this process, only the fibers with homogeneous Ag concentration were selected and used for SXRD. Figure 1(c) exhibited the normalized XRD patterns for x = 0, 0.5, 1.0, and 2.5. The intensity of the main XRD peaks at x = 0.5 and 1.0 decreased to approximately 1/17 times more than that at x = 0, and no changes were observed in all detected XRD peak positions, as is the case with the previous studies.[11-12] The details for XRD results are displayed in **Figure S3(a)-S3(c)**.

However, when Ag was intercalated into $ZrTe_3$ at up to x = 2.5, considerable structural changes were observed. The crystal structure of this novel phase was determined using combinations of single-crystal XRD analysis, Rietveld refinement,[13] transmission electron microscopy (TEM), and density functional theory (DFT) calculations. The trigonal prismatic units in the basic $ZrTe_3$ structure (**Figure 1(d)**) transformed into octahedral units while maintaining 1D order (**Figure 1(e)**). The octahedral unit was found to contain the disorder of Te sites by single-crystal XRD analysis. **Figure S3(d)** and **S3(e)** present the structural analysis results using Rietveld refinement with and without considering the disorder. The $R_{wp}$ factors decreased significantly by considering the Te disorder. The crystal structures and structural parameters were displayed in **Figure S3(f)-S3(g)** and **Table S1-S3**, respectively.

Thus the study found experimental evidence for the previously inferred structural changes from trigonal prismatic to octahedral units.[14] In general, intercalation extends the distance between layers but rarely changes the basic structure of the host material. However, a similar structural change with Ag intercalation into $ZrTe_3$ has also been observed according to the combinations of guest and host, such as Li intercalation into $MoS_2$ [15]. The crystal structures were drawn using the visualization for electronic and structural analysis (VESTA).[16]
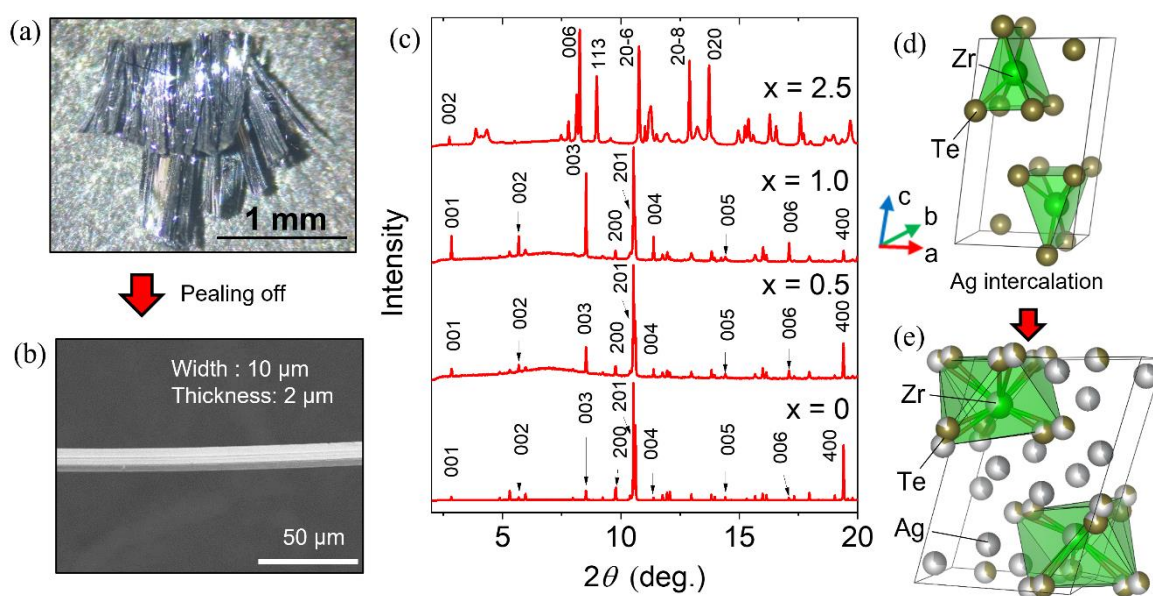
**Figure 1.** (a) Optical image of the as-prepared sample after Ag intercalation. (b) One of the fibrous samples peeled from the as-prepared sample in (a). (c) Normalized synchrotron X-ray diffraction (SXRD) patterns for x = 0, 0.5, 1.0, and 2.5. (d, e) Schematics of crystal structures of (d) $ZrTe_3$ and (e) Ag intercalated $ZrTe_3$ obtained from Rietveld refinement considering the Te disorder.

## 3. Formation of a quasi-amorphous phase

The Ag-intercalated $ZrTe_3$ compounds were analyzed using selected-area electron diffraction (SAED) (**Figure 2(a)–2(f)**) and high-resolution TEM (HRTEM) (**Figure 2(g)–2(l)**). Elemental compositions in each investigated area were measured by scanning TEM (STEM) EDS mapping and were displayed at the top of **Figure 2(a)–2(f)**. Similar to the XRD measurements, despite an increase in the Ag concentration, no considerable changes were observed in the [001] SAED patterns (**Figure 2(a)–2(c)**). **Figure 2(e)** and **2(f)** present the [001] and [100] SAED patterns of the octahedral phase, respectively. Because the *a* lattice constant determined using SXRD considerably increased from 5.89 to 7.65 Å owing to the Ag intercalation, the cleavage in the [100] direction is easier to have occurred with increasing Ag concentration.

In the sample with x = 1.79, complex diffraction spots (**Figure 2(d)**) were observed, indicating a gradual formation of the octahedral phase. During this transition period, the Ag concentration distribution in the nanoscale region was investigated via quantitative point analysis (**Figure S4(a)**). The indicated positions by red crosses in **Figure S4(b)** correspond to the analyzed points. Although the average Ag concentration was x = 1.79, considerable differences in Ag concentrations from x = 1.0 to x = 3.5 were observed in the nanoscale regions. The octahedral phase can structurally accommodate up to six equivalents of Ag when the Ag sites are fully occupied. Then, the experimentally observed maximum Ag concentration from STEM–EDS measurements was x = 4.3 (**Figure S5**). Such a nanoscale Ag

inhomogeneity is a unique feature observed during the structural transition period from trigonal prismatic to octahedral units. Furthermore, the Zr concentration range was 0.7–1.0, indicating the presence of Zr defects.

Note that although an acceleration voltage of 80 keV significantly reduces the beam damage to samples, the influence of the electron beam on the elemental composition remains controversial, as shown in **Figure S6 and S7.** Several other microscope parameters should be considered for further quantitative discussion: beam current, dwell time, sample thickness, and scanning pattern during the STEM observation.

On the other hand, the formation of the Zr defect is consistent with the Rietveld refinement and single crystal structure XRD analyses (**Table S1-S3**). Since these measurement methods do little damage to the sample, the Zr defects would have been inherently introduced due to the charge compensation associated with the Ag introduction. The PDII method introduced a large amount of Ag up to 2.5 equivalents. When the tellurium valence in $ZrTe_3$ becomes -2, monovalent cations can be introduced up to 2 equivalents. Therefore, the contributions of both Zr defects and Te redox should be considered for charge compensation corresponding to the increase in Ag concentration. This research expresses the chemical formula of the final product after Ag intercalation as $Ag_xZr_{1-\delta}Te_3$ (x = 2.5).

The Ag intercalation changed the trigonal prismatic unit into an octahedral unit. However, the transition did not necessitate the reconstruction of the arrangement of each element. It can be achieved by shifting one of the Te sites (Te1A and Te1B in **Table S1-S3**) along the *b*-axis. **Figure 2(m)** shows the gradual change from the trigonal prismatic to the octahedral unit comprising Zr and Te. For simplicity, Te disorder is not shown. Red arrows indicate the shift of Te1 sites along the *b*-axis. **Figure 2(n)–2(q)** also show the gradual change in the *b*-axis projection structures. Thus, a simple shift of the Te sites with variations in the Ag concentration allows the structural transition while maintaining the 1D order. Hence, even though the Ag intercalation changes the basic structure of the host material, the fiber-shaped

body can be maintained, as displayed in **Figure 1(b)**. However, in the intermediate state between trigonal prismatic and octahedral phases, structural distortion, such as the shifting Te site, the change in lattice parameter, and the fluctuation of fractional coordinates of each element, should occur according to the inhomogeneous Ag distribution and disrupt the long-range order despite retention of the 1D order. Herein, this unique amorphous state that maintains the 1D order is referred to as the quasi-amorphous phase.
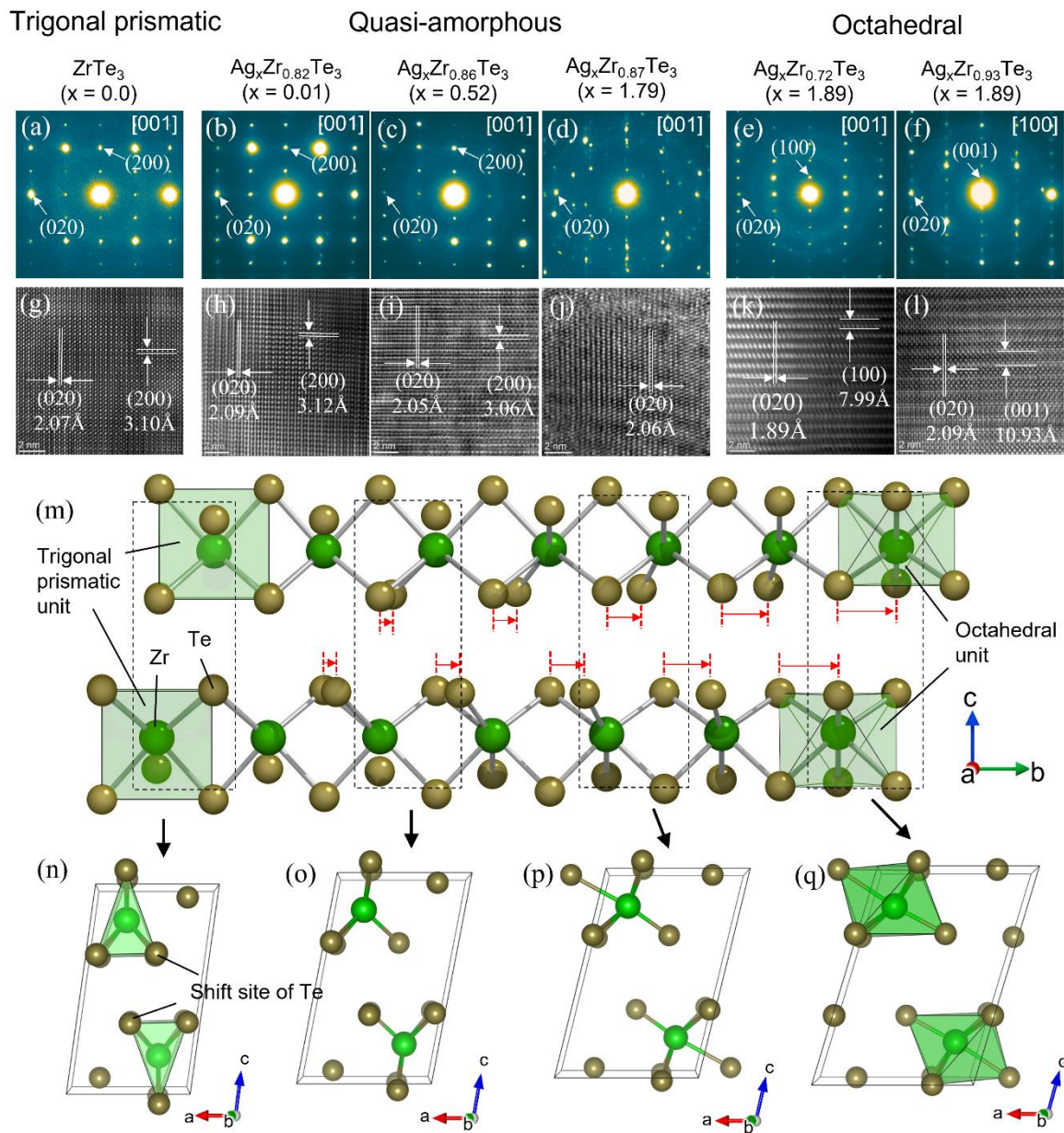


**Figure 2.** (a–f) SAED patterns for (a) trigonal prismatic phase, (b–d) quasi-amorphous phase, and (e, f) octahedral phase. (g–l) HRTEM images corresponding to each sample in (a–f),

8

respectively. (m) Changes in the one-dimensional structure comprising Zr and Te from trigonal prismatic to octahedral phases. Red arrows indicate that Te atoms shift up to half a unit cell along the $b$-axis based on the Ag concentrations. (n–q) Projection structures from the $b$-axis direction during the transformation process.

Thus, Ag intercalated $ZrTe_3$ is composed of three different phases: trigonal prismatic (TP), quasi-amorphous (QA), and octahedral (O) phases. **Figure 3(a)** shows the phase distribution change according to the increased Ag concentration. In the initial state of Ag intercalation, although the QA phase increases, this phase is not reflected in XRD results due to the disruption of long-range order, as observed XRD results for $Ag_xZr_{1-\delta}Te_3$ with x = 0.5 and 1.0 in **Figure 1(c) and S3(c)**. Therefore, the diffraction peaks from only the remaining TP phase with no Ag ions would be detected. Consequently, despite the introduction of Ag, it seemed as if no structural change occurred in the initial state of intercalation. This scenario affords a reasonable explanation for the contradiction that the crystal structure did not change after intercalation.[10-12] In the middle state of intercalation, XRD peak intensity significantly decreases with decreasing the region of the TP phase (**Figure S3(b)**). **Figure 3(b)** also shows the decrease in XRD intensity of the bulk sample after Ag intercalation, and the insets show photo images before and after PDII. The PDII treatment was stopped before the sample was degraded into fibers, as in **Figure 1(a)**. The Average Ag concentration of the sample surface was estimated to be x = 1.4. The detailed results for EDS are described in **Figure S8(e)**. As shown in **Figure 3(c)**, newly appeared broad XRD peaks were assigned to the O phase, indicating the nucleation of this phase. This situation is regarded as the mixing states of the TP, QA, and O phases. For further Ag intercalation, the O phase becomes dominant, and the TP phase disappears (**Figure 1(c)** and **Figure S3(d) and S3(e)**). The relationship between Ag concentration distribution and XRD patterns is displayed in **Figure S8(a) and S8(b)**.

In addition, the nanoscaled Ag distribution in **Figure 3(a)** could not be detected by SEM-

EDS with a resolution of about 1 μm. Even when the Ag concentration can be estimated as x = 1.0 homogeneously by using SEM-EDS, the sample includes regions with and without Ag ions owing to the nanoscale Ag inhomogeneity. On the other hand, the maximum Ag concentration obtained via SEM-EDS was x = 2.6 (**Figure S8(b)**). This value is consistent with the Rietveld refinement results for the XRD pattern of the final product after intercalation. When the average Ag concentration via SEM-EDS approaches x = 2.5, the XRD peaks become sharper (**Figure S8(a)**), and the lattice constant stabilizes, indicating that the nanoscale Ag inhomogeneity is gradually alleviated.
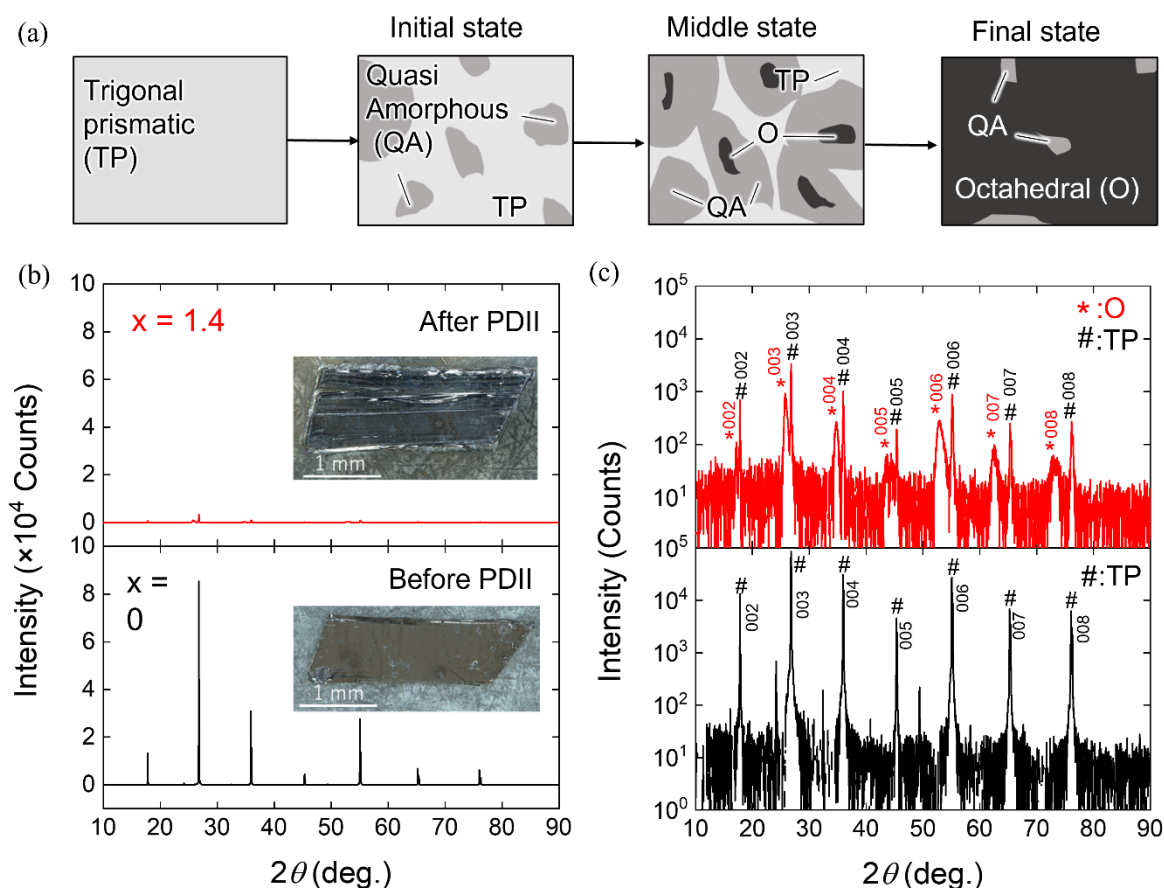


**Figure 3.** (a) The phase distribution change according to the increased Ag concentration. The distribution of three phases: trigonal prismatic (TP), quasi-amorphous (QA), and octahedral (O) phases, alters according to Ag concentration. (b) XRD patterns of the single crystalline sample before and after PDII treatments. Insets show the optical images of samples. (c) the same XRD patterns as (b) with the Y axis on a logarithmic scale. The highly preferred

orientation of (00$l$) was observed in (b) and (c).

## 4. Electronic and superconducting properties in the quasi-amorphous phase

ZrTe$_3$ exhibits filamentary superconductivity below 2 K in nature with no diamagnetism under a small applied magnetic field.[17] An increase in the superconducting transition temperature ($T_c$) has been reported in ZrTe$_3$ compounds with diluted intercalations, such as Ni$_{0.05}$ZrTe$_3$ (3.1 K),[18] Cu$_{0.05}$ZrTe$_3$ (5.2 K),[12] and Ag$_{0.05}$ZrTe$_3$ (5.2 K),[12a] Although this increase in $T_c$ can be understood due to suppressing charge-density waves (CDWs),[19] the coexistence of bulk superconductivity and CDWs have also been reported. [12b, 18, 20]

The electrical properties of the fibrous samples with different Ag concentrations (x = 0, 0.5, 1.0, 2.0, and 2.5) were investigated. Because the samples showed nanoscale Ag inhomogeneity, the described x was the average value obtained from the SEM–EDS measurements. The metallic conducting behavior for x = 0 changed to semiconducting for x = 2.5. At the intermediate Ag concentrations, the metallic ZrTe$_3$ phase and semiconducting Ag$_{2.5}$Zr$_{1-\delta}$Te$_3$ phase are mixed, as in the Ag distribution in **Figure 3(a)**, resulting in the continuous change in resistivity with increasing Ag concentration. The resistivity could be modulated from 0.216 to 266 mΩ cm at room temperature and from 0 to 788 mΩ cm at the lowest temperature (**Figure 4(a)**). When x = 0.5, the maximum $T_c$ was obtained at 6.3 K among the $MX_3$-related intercalation compounds, indicating the sharp drop at $T_c$ in **Figure 4(b)**. The negative susceptibility derived from the superconductivity was also confirmed in **Figure S9(a)**.

The upper-critical magnetic field ($B_{c2}$) was measured for the sample with x = 0.5. When the magnetic field ($H$) was applied parallel to the $a$- and $c$-axes (**Figure S9(b)** and **S9(c)**), $B_{c2}(0)$ values were estimated to be 12 and 5 T, respectively, indicated by the dashed lines based on the straight-line approximation in **Figure 4(c)**. Similarly, the $B_{c2}(0)$ value of <2 T was previously reported for polycrystalline Ag$_{0.05}$ZrTe$_3$.[12a] In single-crystalline Cu$_{0.05}$ZrTe$_3$ ($T_c$ =

3.8 K), the $B_{c2}(0)$ value was ~4.5 T[12b] when the resistivity in the $T_c$ onset was adopted as a criterion for $B_{c2}$. Therefore, $Ag_{0.5}Zr_{1-\delta}Te_3$ with mixing state of TP and QA phases showed remarkable robustness against the magnetic field.

Due to the disordered structure, the QA phase is expected to suppress the CDW. In general, the suppression of CDW contributes to an enhancement of superconductivity because the electrons trapped on CDW are released. Based on the Ag distribution in **Figure 3(a)**, the mixing state of TP and QA phases in the initial state of Ag intercalation can qualitatively explain the coexistence of superconductivity and CDWs, as discussed in the previous studies.[12b, 18, 20] In addition, if the nanoscaled regions of the QA phase function as the effective pinning center, the nanoscaled Ag inhomogeneous distribution has the potential to enhance the upper critical field.
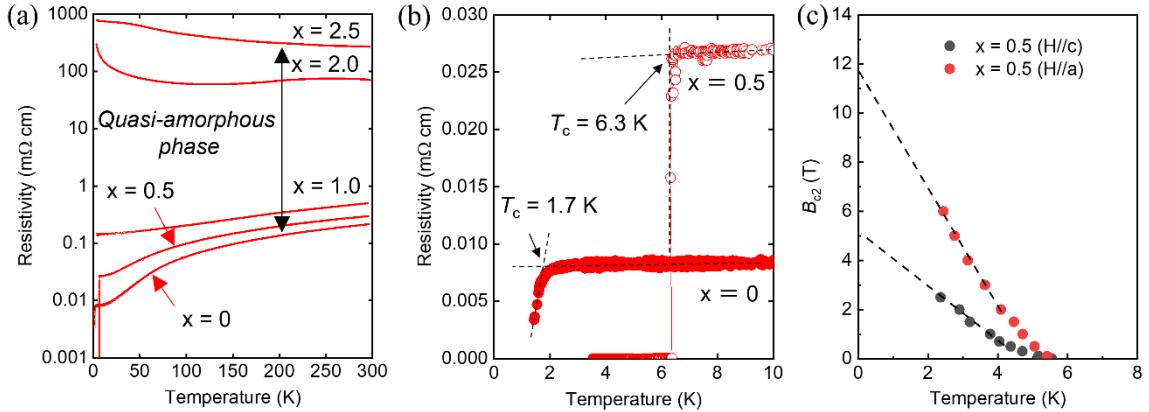


**Figure 4.** (a) Temperature dependence of resistivity for x = 0, 0.5, 1.0, 2.0, and 2.5. (b) Expanded view of (a) at 0–10 K. (c) Upper-critical magnetic field for x = 0.5. The applied magnetic field is parallel to the *a-* and *c-*axes, and the dotted lines denote the straight-line approximation.

## 5. Mechanism forming the quasi-amorphous phase

In this section, the interaction between Ag ions was investigated to reveal the origin of the QA phase formation through the DFT calculations. At the initial state of intercalation, the

crystal structure after a small amount of Ag introduction should be close to the pristine $ZrTe_3$. Therefore, a TP phase was used as the initial structure, and the most stable positions for Ag ions within the structure were founded. The detailed explanations for finding the stable sites are described in **Figure S10**. The three stable sites for Ag ions are shown in **Figure 5(a)**, which are located inside the tetrahedral (T), pyramidal (P), and square (S) spaces formed by Te atoms.

The interaction between Ag ions was investigated using the supercell ($3 \times 5 \times 1$) of $Zr_{30}Te_{90}$ with two additional Ag ions. In **Figure 5(b)**, the first Ag ion was placed at the T site in the supercell as indicated by the red atom, and the second Ag ion was added to each different position as indicated by the numbers from 1 to 12 in black. Thus, the twelve configurations after ionic relaxation were depicted in the same Figure (**Figure 5(b)**). The darker the blue color of the second Ag ion, the lower the total energy. Except for positions 2 and 4 of the P sites, the second Ag ion hardly moved from the initial position even after relaxation. **Figure 5(c)** shows the difference in total energy ($\Delta E$) between the most stable configuration and each configuration as a function of the distance between Ag ions. When Ag ions approached each other, $\Delta E$ decreased, indicating attraction between Ag ions in the van der Waals gap. The most stable configurations were obtained when Ag ions were placed at position 2 initially. Through the ionic relaxation, Ag ions at positions 2 and 4 moved to position 3. At the same time, nearby Te ions spread along the $c$-axis, forming the stable space for Ag ions, as indicated by red arrows (**Figure 5(d)**). This movement of Te is considered to be the origin of the attraction between Ag ions. Furthermore, when the Ag ions were arranged at S and T sites alternatively based on their interaction, a commensurate superstructure with the modulation vector $q = (0, 1/3, 0)$ was obtained from DFT calculations (**Figure S10(h)**). In addition, the case where the first Ag ion was placed at the S site was also investigated in **Figure S11(a)-S11(c)**.

In typical 2D materials, intercalated ions move away from each other because of Coulomb repulsion. Therefore, guest ions should be distributed throughout the interlayers, expanding

the $c$-lattice parameter. The interactions between Ag ions in TMDs ($TiS_2$, $TaS_2$, and $NbSe_2$) with the 2D structure were investigated via DFT calculations; it has been reported that these intercalation compounds can be synthesized experimentally.[5, 7b, 21] When Ag ions were the farthest away from each other, the most stable state could be obtained in TMDs (**Figure S16 and S17(b), S17(c), and S17(e)**). Thus, the attraction between cations in $ZrTe_3$ is unusual among intercalation compounds. Such a force locally concentrates the Ag ions and works as the origin of the nanoscaled Ag inhomogeneity, resulting in a QA phase formation.

However, the microscale SEM–EDS measurements confirmed that Ag was uniformly distributed throughout the sample in the intermediate concentration region of x = 0.5 and 1.0 (**Figure S2**). This situation cannot be explained by only the attraction between Ag ions. Therefore, Ag ion diffusivity in the van der Waals gaps was also investigated using the $AgZr_{18}Te_{54}$ supercell ($3 \times 3 \times 1$). **Figure S12(c)** shows the activation energy ($\Delta E_a$) for Ag diffusion along the $a$- and $b$-axes using the nudged elastic band (NEB) method. Each diffusion path for Ag ion is shown in **Figure S12(a)** and **S12(b)**. The calculated $\Delta E_a$ along the $a$- and $b$-axes were 0.6 and <0.05 eV, respectively. Therefore, a high anisotropic Ag diffusion is expected.

Furthermore, to consider the interaction between Ag ions, single and pair diffusion processes along the $b$-axis were modeled using the $Ag_2Zr_{18}Te_{54}$ supercell ($3 \times 3 \times 1$). One of the Ag ions was fixed at the T site, and the other was diffused alone in **Figure 5(e)**. Also, In **Figure 5(f)**, two Ag ions were placed at T and S sites, and then they diffused together while maintaining a certain distance. Although the $\Delta E_a$ of single diffusion was around 0.3 eV, that of pair diffusion reduced to < 0.05 eV (**Figure 5(g)**). This difference in $\Delta E_a$ corresponds to the required energy to separate Ag ions, supporting the local attraction between Ag ions. Furthermore, $\Delta E_a$ of pair diffusing is comparable to that in the case of single diffusion without Ag interaction (**Figure S12(c)**). The case where the Ag ion was fixed at the S site was also investigated (**Figure S11(d)-S11(f)**). In both cases, the fast Ag diffusion can be expected along the $b$-axis. Note that

further investigations should be necessary for the possibility of triple or multiple diffusion.

Therefore, during the PDII treatment at 150 °C, Ag ions were immediately and uniformly distributed along the longitudinal fiber direction owing to their low activation energy, as demonstrated by the EDS mapping image in **Figure S2(f)**. Uniformly distributed Ag ions were locally concentrated due to their attraction after PDII treatment. This scenario can explain the nanoscale inhomogeneity observed from STEM–EDS measurements, despite the microscale homogeneity observed from SEM–EDS measurements. Note that a visible decomposition could not be confirmed even when the sample was left in air for several months.
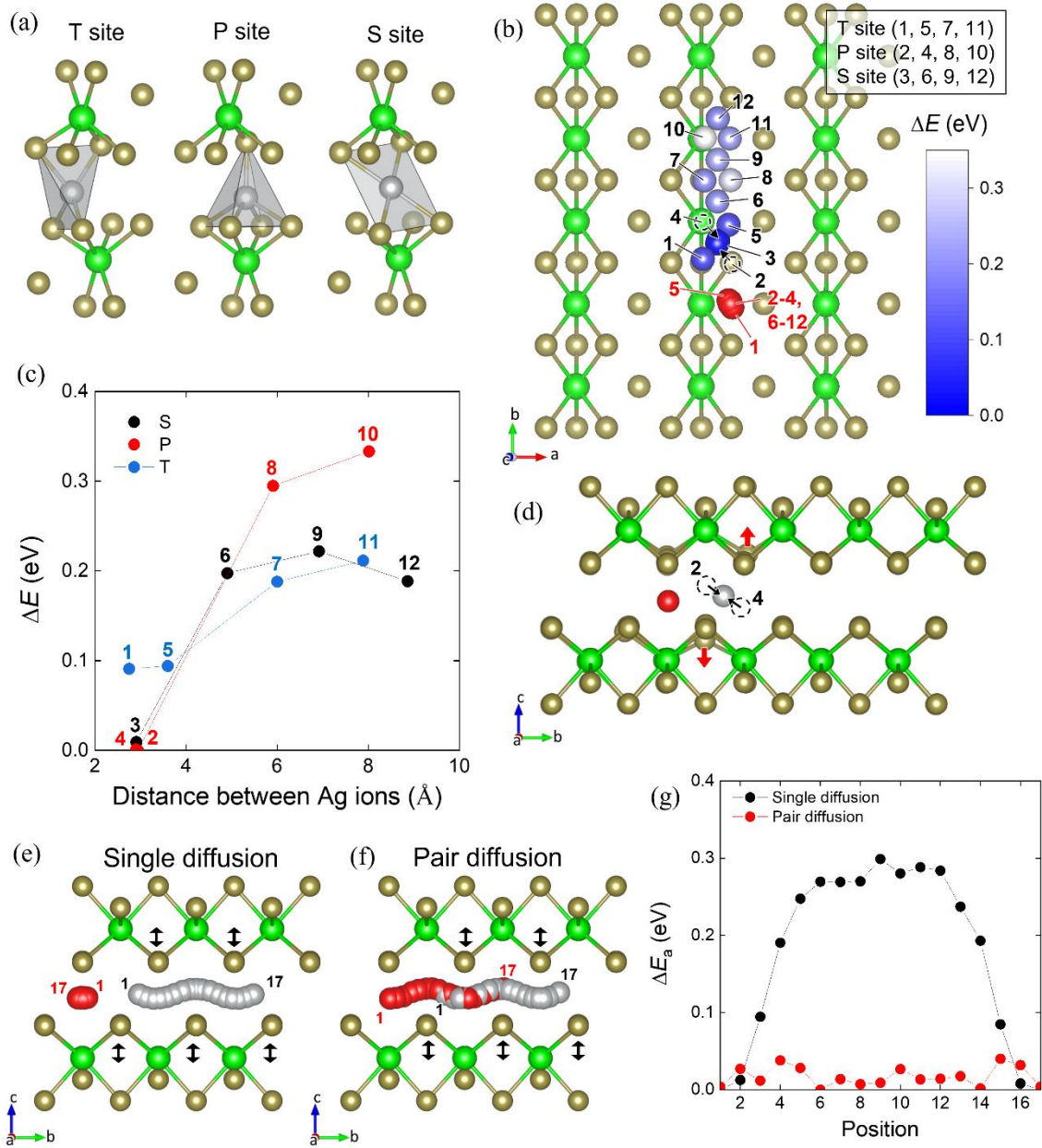
**Figure 5** (a) Three stable sites of an Ag ion in $ZrTe_3$. (b) Energetically stable positions of the second Ag ion in a $Ag_2Zr_{30}Te_{90}$ supercell ($3 \times 5 \times 1$). The first Ag ion is placed at the T site, as indicated by the red atom. The second Ag ion is placed at S, P, and T sites each, denoted by 3, 6, 9, and 12 for S, 2, 4, 7, and 11 for P, and 1, 5, 8, and 10 for T. Twelve configurations after ionic relaxation are depicted in the same Figure (b). The difference in total energy ($\Delta E$) between the most stable configuration, where the second Ag ion is placed at position 2, and each other configuration is shown by the color of the second Ag ion. The darker the blue color, the more

stable the configuration. (c) Local attraction as a function of the distance between Ag ions. (d) Migration of Ag ions to the S site from the adjacent P sites. (e, f) Ag ion paths with the interaction between Ag ions for the (e) single diffusion and (f) pair diffusion along the *b*-axis using the nudged elastic band (NEB) method. (g) Activation energy ($\Delta E_a$) for single (e) and pair (f) diffusions of Ag ions.

## 6. Overview of the TMT intercalation compounds

**Figure 6** presents an overview of the TMT intercalation compounds. One valuable achievement of the solid-state intercalation process using PDII was that the final product of TMT intercalation compounds was experimentally shown to exhibit a 1D structured O phase. So far, various $A_xMX_3$ compounds, such as $Tl_2ZrS_3$,[22] $Tl_2HfSe_3$,[22] $Cu_2MTe_3$ (M = Ti, Zr, and Hf),[23] $A_2ZrSe_3$ (A = K and Rb),[24] $Na_2ZrS_3$,[25] $K_{1.33}TiTe_3$,[26] $BaTaS_3$,[27] and $TlTaX_3$ (X = S and Se),[28] have been synthesized via solid-state reactions. These compounds comprise 1D structured O units with six coordinated chalcogens centered on transition metals, identical to the O phase of $Ag_{2.5}Zr_{1-\delta}Te_3$ prepared via Ag intercalation. Specifically, the basic frameworks of $Ag_{2.5}Zr_{1-\delta}Te_3$ and $Tl_2MX_3$ are similar. These findings suggest that TMTs and the reported $A_xMX_3$ compounds via solid-state reactions can be categorized into the same family; the latter can be regarded as the final products after intercalation into the former.

Furthermore, as mentioned previously, $A_{0.05}ZrTe_3$ (A = Ag, Cu, Ni, Fe) with diluted guest ions could have been reported.[10-12] They can be recognized as the QA phase because of their XRD results. Whether all the formed QA phases will reach the O phases via further ion intercalation is unclear; however, the continuous structural changes from the TP to the O units with an increase in the ion concentration should pass through such a QA phase. In particular, Cu intercalation into $ZrTe_3$ is expected to form the O phase via a QA phase. Thus far, single crystal growth of $Cu_2ZrTe_3$ with the O phase[23] and an electrochemical Cu intercalation into $ZrTe_3$ using a liquid-phase process[29] have been reported. Although the detailed crystal

structure of Cu intercalated $ZrTe_3$ has been unknown, the Cu concentrations of final products via both methods are almost comparable: 1.9 equivalents for Cu intercalation and 2.0 equivalents for single crystal growth. At the current stage, it is necessary to elucidate the crystal structure, but the Cu intercalation via solid-state intercalation will afford clearer conclusions, as with Ag intercalation.

The structural change to the O phase via the QA phase is vastly different from that observed in the usual case of 2D materials with an expansion of the $c$ lattice constant and can be recognized as a feature of TMT intercalation. However, based on the combination of the parent compound and guest ions, TMT can also exhibit the same structural changes as 2D materials. **Figure S15(c)** and **S15(f)** show the crystal structure of $A_xZrSe_3$ (A = K, Rb, and Cs), which exhibits a layered structure comprising TP units and A ions sandwiched between their layers. These compounds have been synthesized via a solid-state reaction[30] and an intercalation reaction using metal ammonia solutions[31]. In addition, DFT calculations also could reproduce the experimentally reported crystal structure of $A_xZrSe_3$ (A = K, Rb, and Cs) from TMT-structured $ZrSe_3$ **(Figure S14** and **S15)**. Therefore, two cases of structural changes could occur via guest ion intercalation into TMT: in the first case, the basic crystal structure changes to an O phase via a QA phase, and in the second case, guest ions are accommodated between layers, and then the $c$-axis length is extended while maintaining the TP structure.

Here, the interactions between guest ions were investigated in the case of $A_xZrTe_3$ (A = Ag, Cu, Ni, and Fe), which showed a QA phase, and $A_xZrSe_3$ (A = K, Rb, and Cs), which retained its TP structure. **Figure 6(a)** shows the difference in the total energy between configurations where the guest ions were placed adjacent to each other at the closest position and where the guest ions were placed at the same site of the second closest position. The detailed configurations and calculation conditions are described in **Figure 5(b), S13, and S17**. Similar to Ag ions, the attraction was observed between other guest ions in the cases of $A_xZrTe_3$ (A = Cu, Ni, and Fe), where the QA phase was formed. Furthermore, a repulsive force was

observed between the ions in $A_xZrSe_3$ (A = K, Rb, Cs), where the *c*-axis length is extended while maintaining the structure. Thus, the interactions between guest ions would be an index for predicting the structure of the final compound after intercalation. The overall details of these TMT intercalation compounds can be revealed more clearly by investigating each material individually.
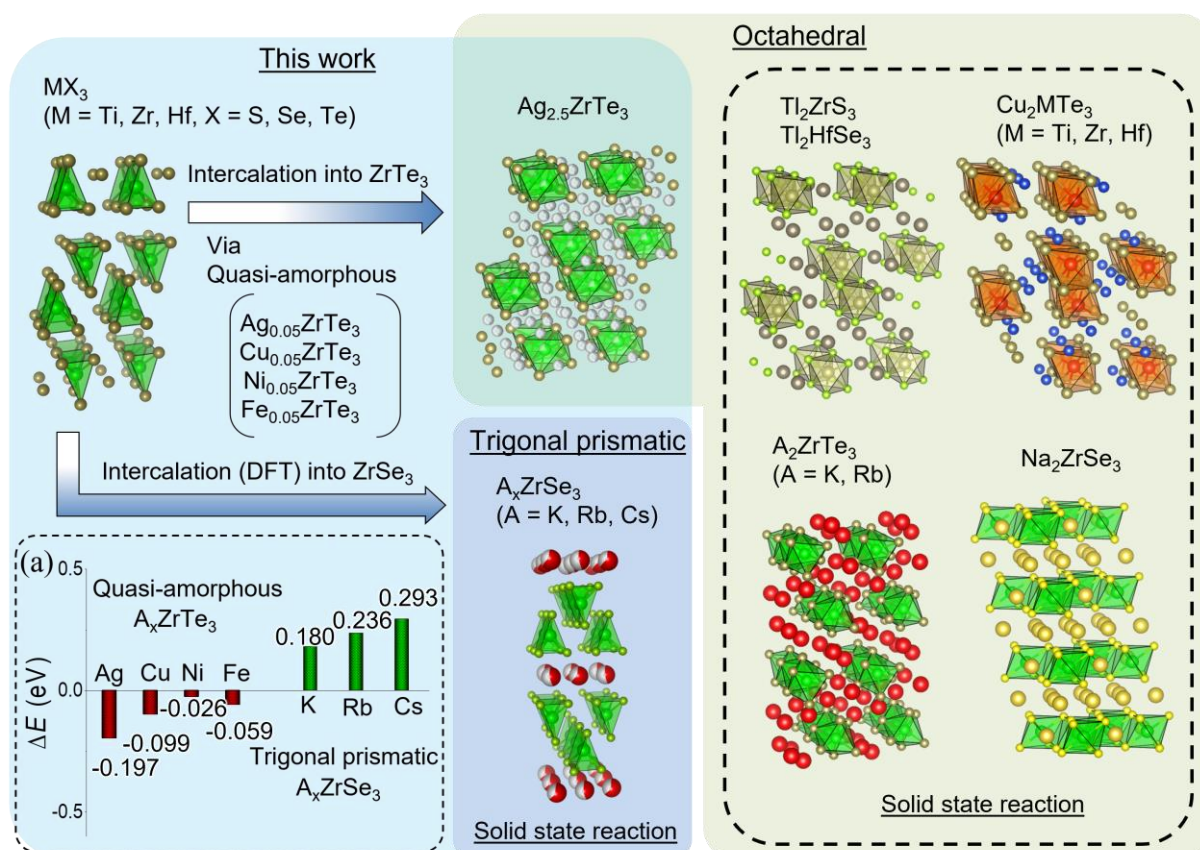


**Figure 6.** (a) Interaction between guest ions in the cases of $A_xZrTe_3$ (A = Ag, Cu, Ni, and Fe) and $A_xZrSe_3$ (A = K, Rb, and Cs). When the interaction between guest ions is attraction, a QA phase is expected to be formed. Alternatively, repulsion between guest ions will induce a simple lattice expansion while maintaining the TP structure. The reported $A_xMX_3$ compounds obtained via the solid-state reaction show a 1D structured O phase. This is the same structure of the final product obtained from the Ag intercalation into $ZrTe_3$ with a 1D structure TP phase. Such a structural change should pass through the QA phase and is vastly different from

that observed in the case of 2D materials based on general intercalation. This is one of the unique features of TMT intercalation compounds.

## 7. Conclusions

Ag intercalation into $ZrTe_3$ transformed the original 1D structured TP phase into a 1D structured O phase: a novel metastable phase. This structural change can be easily achieved by shifting one Te site along the $b$-axis while maintaining the 1D order. However, in this transition period, the highly inhomogeneous Ag concentration was confirmed in the nanoscaled area using STEM-EDS measurements. Because the structural distortion should be induced based on variations in the Ag concentration in the nanoscale region, the long-range order of crystals should be disrupted, despite the retention of the 1D order. Such a state is referred to as a QA phase in this study.

DFT calculations indicated that the nanoscale Ag inhomogeneity originated from the attraction between guest ions. This attraction also causes the pair diffusion of Ag ions in $ZrTe_3$: Ag ions diffuse in the same direction at constant intervals. In addition, the NEB method predicted the fast ion diffusion with $\Delta E_a < 0.05$ eV along the $b$-axis. These features can explain the coexistence of microscale Ag homogeneity and nanoscale Ag inhomogeneity observed in SEM and STEM-EDS measurements.

Even when one equivalent of homogeneous Ag concentration was detected in the macroscopic region of the sample, the small area with no Ag concentration equivalent to the parent compound was included in the sample due to the nanoscale Ag inhomogeneity. Since the XRD and TEM patterns were reflected only from the region with the long-range order, it seemed as if no structural change occurred even after intercalation.

According to the Ag concentration, the electric properties of $Ag_xZr_{1-\delta}Te_3$ changed continuously from superconductivity to semiconductivity. The maximum average Ag concentration was x = 2.5, and the resistivity could be modulated from 0.216 to 266 mΩ cm at

300 K. Furthermore, when the Ag concentration is x = 0.5, the highest $T_c$ and $B_{c2}$ were obtained. The mixing state of TP and QA phases with nanoscale Ag inhomogeneity should induce a randomly distributed non-superconducting region with a high Ag concentration, which could function as an effective pinning center. This scenario also can qualitatively explain the coexistence of bulk superconductivity and CDWs.

Furthermore, an overview of TMT intercalation compounds based on the findings of this research was presented. The interaction between guest ions can be a valuable indicator for predicting the final products of TMT intercalation compounds. The findings of this research suggested that TMTs and the reported $A_xMX_3$ compounds can be categorized into the same family. Since the various guest species could be flexibly accommodated in the three-dimensional spread van der Waals gap, many compounds are expected to belong to this family. In particular, the QA phase with 1D order is the state of matter based on a novel concept. It has the potential to open a pathway to achieve high functionality, such as fast ion diffusivity for low activation energy, a low thermal conductivity derived from the phonon scattering in a QA state, and high controllability of the electric carrier density based on the high guest-ion accommodation capacity.

## 8. Method

### 8.1. Sample preparation for single-crystalline ZrTe₃

Single-crystal $ZrTe_3$ was prepared using a chemical vapor transport method. A mixture of polycrystal powdered $ZrTe_3$ and $I_2$ (5 mg/cm³) was placed in an evacuated quartz tube and heated at a temperature gradient between 800°C and 900°C for seven days.

### 8.2. Ag intercalation into ZrTe₃

The schematic configuration of PDII and the expected chemical formulas are shown in **Figure S1(a)**. AgI was adopted as an Ag ion source of the solid electrolyte owing to its high

$Ag^+$ conductivity and placed on ZrTe$_3$. PDII was performed in a 100% H$_2$ atmosphere at 150°C. When voltage was applied between the needle-shaped anode and carbon cathode, a corona discharge occurred at the edge of the former. The hydrogen molecules ionized to protons, which were then irradiated to AgI. On the AgI surface, protons drove the $Ag^+$ and reacted with the I$^-$. The generated HI should then be evaporated as a gas. The $Ag^+$ should also be discharged from the bottom side of AgI to compensate for the charge neutrality of the solid electrolyte. On the other hand, the electrons generated at the anode flow through the electric circuit to ZrTe$_3$. When ZrTe$_3$ received these electrons and discharged the $Ag^+$ from AgI, the intercalation reaction proceeded as per the chemical formula in **Figure S1(a)**. The representative synthesis condition for Ag$_x$Zr$_{1-\delta}$Te$_3$ is shown in **Figure S1(b)**. The PDII method gradually introduced Ag ions from the top side of single-crystal ZrTe$_3$. Thus, the Ag concentration at the interface between AgI and ZrTe$_3$ should be considerably higher than that at the bottom side of ZrTe$_3$. Therefore, fibers with different Ag concentrations can be obtained from the same lump of Ag$_x$Zr$_{1-\delta}$Te$_3$. However, a fully occupied sample can be obtained by adjusting the sample mass or treating it for an extended period. Details of the ion introduction mechanism have been demonstrated in a previous report.[7a]

## 8.3. Analysis of elemental composition and electron diffraction measurements

The elemental composition in the microscale regions was analyzed in **Figure S2** and **S8** using SEM-EDS (JEOL, JCM-6000). TEM samples were prepared by mechanical exfoliation and dropped onto a perforated amorphous carbon film supported Mo microgrid (EM Japan, Co., Ltd). Observation and STEM-EDS at different operation voltages (80 kV, 200 kV) were performed with JEOL ARM-200F, and 1250 keV observation was carried out with JEOL ARM-1300: **Figure 2(a)–2(l)**, **S4** and **S5** (80 kV), **Figure S6(a)** and **S6(c)–S6(j)** (200 kV), and **Figure S6(b)** (1250 kV). Note that electron irradiation by TEM analysis may affect the state of samples depending on the applied voltage.[32] However, it was confirmed that the

application of 80 keV did not show the time dependence of change in the SAED patterns or elemental compositions even when the same area is irradiated for a long time. The detail is described in **Figure S6 and S7**.

### 8.4. Structural characterization using XRD

The crystal structure of $Ag_xZr_{1-\delta}Te_3$ was investigated by SXRD measurements on a BL02B2 experimental station of SPring-8 (JASRI; Proposal 2015A1441), laboratory-scale XRD measurements (Rigaku; MiniFlex600 with D/teX Ultra), and single-crystal XRD analysis (Rigaku; XtaLab Synergy diffractometer with a single microfocus Mo Kα X-ray radiation source (PhotonJet-S), equipped with a hybrid pixel array detector (HyPix-6000HE)). CrysalisPRO (Rigaku Oxford Diffraction, 2017) software was used for data collection, cell refinement, and data reduction of single-crystal XRD analysis. SHELXT software[33] was used to solve the initial structure and the structural refinement was performed by SHELXL2018/3 [34] which were compiled into OLEX2. [35]

The single-crystal fine fibers were peeled off one by one from the lump of $Ag_xZr_{1-\delta}Te_3$ comprising regions of different Ag concentrations. Based on SEM–EDS measurements, each fiber with homogeneous Ag concentration was analyzed to investigate the structural changes in the samples under different Ag concentrations. Then, several fibers were placed directly into capillary glass tubes. The SXRD results of these fibers with x = 0, 0.5, 1.0, and 2.5 are shown in **Figure 1(c).** Furthermore, to determine the crystal structure of the final product after Ag intercalation, the sample with x = 2.5 was mixed with a small amount of quartz and ground together to avoid the preferred 1D orientation. The obtained powder was filled in capillary glass tubes and analyzed (**Figure S3(a)**). SXRD measurements were conducted at ambient temperature. The wavelength of the radiation beam used was 0.495813 Å. The fibers were also evaluated on laboratory-scale XRD measurements (**Figure 3** and **S8**). The flexible fibrous bodies were fixed by cleaving the single-crystal samples many times on adhesive tape

on a flat glass plate, and the *c*-axis oriented surface was exposed (**Figure S8(c)** and **S8(d)**).

## 8.5. Evaluation of electric and magnetic properties

The temperature dependencies of the resistivities for the samples with different x values were measured using a refrigeration system (Thermal Block Company, SB-1.5KCRS0.5-TRB) (**Figure 4(a)** and **4(b)**). The resistivity measurements under a magnetic field were performed using a physical property measurement system (Quantum Design) to determine the upper-critical magnetic field ($B_{c2}$) (**Figure S9(b)** and **S9(c)**). A resistivity of 90% at the $T_c$ onset was adopted as a criterion for estimating the $B_{c2}$ level (**Figure 4(c)**). A magnetic property measurement system (Quantum Design) was employed to estimate the magnetic susceptibility (**Figure S9(a)**).

## 8.6. DFT calculations

For all calculations, the projector augmented wave method in the Vienna ab initio simulation package[36] and the generalized gradient approximation (Perdew–Burke–Ernzerhof approximation[37]) as the exchange-correlation functional were employed.

### 8.6.1. Exploring energy landscapes for Ag ion in a ZeTe₃ unit cell

The plane-wave cutoff energy was 300 eV. The Brillouin zone (BZ) was sampled using a 4 × 6 × 2 Monkhorst-pack grid and integrated using the tetrahedron method with Blöchl correction (**Figure S10(a)**).

### 8.6.2. Relaxation of the supercell (3 × 3 × 1) of $Ag_xZr_{18}Te_{54}$ (x = 1, 2) and (3 × 5 × 1) of $A_2Zr_{30}Te_{90}$ (A = Ag, Cu,)

The plane-wave cutoff energy was 450 eV, and a single *k*-point at (0, 0, 0) was used for the BZ sampling. In addition, Gaussian smearing with $\sigma = 0.04$ was employed. Ionic positions were relaxed until Hellmann–Feynman forces were reduced to <0.03 eV/Å while fixing the

lattice parameters. **Table S4** summarizes the employed lattice parameters. The DFT-D3 method was employed to estimate the van der Waals force (**Figure 5(b), 5(c), 6(a), S10(e), S10(g), S11(a)-S11(c),** and **S13**).

### 8.6.3. NEB method for Ag migration in $Zr_{18}Te_{54}$ with and without interaction between Ag ions

The plane-wave cutoff energy was 450 eV, and a single *k*-point at (0, 0, 0) was used for the BZ sampling. In addition, Gaussian smearing with $\sigma = 0.04$ was employed. The ionic positions were relaxed until the Hellmann–Feynman forces were reduced to <0.03 eV/Å. The lattice parameters were fixed based on **Table S4**. The DFT-D3 method was employed to estimate the van der Waals force (**Figure 5(e)-5(g), S11(d)-S11(f)**, and **S12(a)-S12(c)**).

### 8.6.4. Relaxation of the supercells (3 × 3 × 1) of $A_xZr_9Se_{27}$, (3 × 3 × 2) of $A_xZr_{36}Se_{108}$, and (3 × 4 × 1) of $A_xZr_{18}Se_{54}$ (A = K, Rb, and Cs), (3 × 3 × 1) of $Ag_xM_{18}X_{36}$, and (4 × 4 × 1) of $Ag_xM_{32}X_{64}$ (M = Ti, Ta, and Nb; X = S and Se), and (3 × 3 × 1) of $A_xZr_{18}Te_{54}$ (A = Ni, and Fe)

The plane-wave cutoff energy was set to 450 eV, and a single *k*-point at (0, 0, 0) was used for the BZ sampling. Furthermore, Gaussian smearing with $\sigma = 0.04$ was employed. The ionic positions and lattice parameters were relaxed until Hellmann−Feynman forces were reduced below 0.03 eV/Å. The DFT-D3 method was employed to consider the van der Waals force. Spin polarization was also considered in the calculations for configurations involving Ni and Fe. (**Figure. 6(a), S14, S15, S16**, and **S17**)

Further details of the crystal structure investigations may be obtained from the Fachinformationszentrum Karlsruhe, 76344 Eggenstein-Leopoldshafen (Germany), on quoting the depository number CSD- 2218957.

**Supporting Information**
Supporting Information is available from the Wiley Online Library or from the author.

Received: ((will be filled in by the editorial staff))
Revised: ((will be filled in by the editorial staff))
Published online: ((will be filled in by the editorial staff))

References

[1]     A. Patra, C. S. Rout, *RSC Advances* **2020**, 10, 36413.

[2]     a)Y. Onuki, R. Inada, S. Tanuma, S. Yamanaka, H. Kamimura, *Solid State Ionics* **1983**, 11, 195; b)E. Canadell, C. Thieffry, Y. Mathey, M. H. Whangbo, *Inorganic Chemistry* **1989**, 28, 3043.

[3]     J. Xia, J. Wang, D. Chao, Z. Chen, Z. Liu, J. L. Kuo, J. Yan, Z. X. Shen, *Nanoscale* **2017**, 9, 7533.

[4]     a)T. Matsuyama, A. Hayashi, T. Ozaki, S. Mori, M. Tatsumisago, *J Ceram Soc Jpn* **2016**, 124, 242; b)T. Matsuyama, A. Hayashi, T. Ozaki, S. Mori, M. Tatsumisago, *J Mater Chem A* **2015**, 3, 14142.

[5]     K. Zagarzusem, M. Fujioka, T. Shibuya, S. Demura, S. Adachi, Y. Takano, M. Jeem, M. Ono, H. Kaiju, J. Nishii, *2D Materials* **2020**, 8.

[6]     R. R. Chianelli, M. B. Dines, *Inorganic Chemistry* **1975**, 14, 2417.

[7]     a)M. Fujioka, C. Wu, N. Kubo, G. Zhao, A. Inoishi, S. Okada, S. Demura, H. Sakata, M. Ishimaru, H. Kaiju, J. Nishii, *J Am Chem Soc* **2017**, 139, 17987; b)M. Fujioka, N. Kubo, M. Nagao, R. Msiska, N. Shirakawa, S. Demura, H. Sakata, H. Kaiju, J. Nishii, *J Ceram Soc Jpn* **2018**, 126, 963.

[8]     S. Iwasaki, H. Morito, T. Komine, K. Morita, T. Shibuya, J. Nishii, M. Fujioka, *Adv Mater* **2021**, e2106754.

[9]     S. Furuseth, H. Fjellvåg, L.-G. Johansson, V. P. Gultyai, I. Persson, L. I. Elding, *Acta*

*Chemica Scandinavica* **1991**, 45, 694.

[10]    C. Mirri, A. Dusza, X. Zhu, H. Lei, H. Ryu, L. Degiorgi, C. Petrovic, *Phys Rev B* **2014**, 89.

[11]    C. S. Yadav, P. L. Paulose, *AIP Conference Proceedings* **2012**, 1447, 895.

[12]    a)C. S. Yadav, P. L. Paulose, *J Phys Condens Matter* **2012**, 24, 235702; b)X. Zhu, H. Lei, C. Petrovic, *Phys Rev Lett* **2011**, 106, 246404.

[13]    F. Izumi, K. Momma, *Solid State Phenomena* **2007**, 130, 15.

[14]    D. W. Murphy, F. A. Trumbore, *J Electrochem Soc* **1976**, 123, 960.

[15]    M. A. Py, R. R. Haering, *Can J Phys* **1983**, 61, 76.

[16]    K. Momma, F. Izumi, *J Appl Crystallogr* **2011**, 44, 1272.

[17]    H. Nakajima, K. Nomura, T. Sambongi, *Physica B & C* **1986**, 143, 240.

[18]    H. Lei, X. Zhu, C. Petrovic, *EPL (Europhysics Letters)* **2011**, 95.

[19]    S. L. Gleason, Y. Gim, T. Byrum, A. Kogar, P. Abbamonte, E. Fradkin, G. J. MacDougall, D. J. Van Harlingen, X. D. Zhu, C. Petrovic, S. L. Cooper, *Phys Rev B* **2015**, 91.

[20]    A. M. Ganose, L. Gannon, F. Fabrizi, H. Nowell, S. A. Barnett, H. Lei, X. Zhu, C. Petrovic, D. O. Scanlon, M. Hoesch, *Phys Rev B* **2018**, 97.

[21]    a)O. S. Rajora, A. E. Curzon, *physica status solidi (a)* **1986**, 97, 65; b)G. A. Scholz, R. F. Frindt, *Mater Res Bull* **1980**, 15, 1703; c)R. A. Yakshibaev, V. N. Zabolotskii, R. F. Almukhametov, *Physica Status Solidi (a)* **1989**, 111, 431.

[22]    C. R. Sankar, B. A. Kuropatwa, A. Assoud, H. Kleinke, *Dalton Trans* **2012**, 41, 9646.

[23]    P. M. Keane, J. A. Ibers, *Journal of Solid State Chemistry* **1991**, 93, 291.

[24]    K. O. Klepp, A. Kolb, *Zeitschrift Fur Naturforschung Section B-a Journal of Chemical Sciences* **1999**, 54, 441.

[25]    F. Lissner, T. Schleid, *Zeitschrift für anorganische und allgemeine Chemie* **1999**, 625, 195.

[26]    A. Kolb, K. O. Klepp, *Zeitschrift Fur Naturforschung Section B-a Journal of*

*Chemical Sciences* **2003**, 58, 633.

[27]    R. A. Gardner, M. Vlasse, A. Wold, *Inorganic Chemistry* **1969**, 8, 2784.

[28]    a)C. L. Teske, W. Bensch, A. Perlov, H. Ebert, *Zeitschrift für anorganische und allgemeine Chemie* **2002**, 628; b)C. L. Teske, W. Bensch, D. Benea, J. Minár, A. Perlov, H. Ebert, *Zeitschrift für Naturforschung B* **2005**, 60, 858.

[29]    W. Finckh, C. Felser, W. Tremel, G. Ouvrard, *J Alloy Compd* **1997**, 262, 97.

[30]    K. O. Klepp, N. A. Harringer, A. Kolb, *ChemInform* **2003**, 34.

[31]    M. Elgaml, S. J. Cassidy, S. J. Clarke, *J Sol St Chem* **2022**, 314, 123436.

[32]    a)R. Li, X. Xu, B. Zhu, X. Y. Li, Y. Ning, R. Mu, P. Du, M. Li, H. Wang, J. Liang, Y. Chen, Y. Gao, B. Yang, Q. Fu, X. Bao, Nat Commun 2021, 12, 1406; b)A. K. Geremew, S. Rumyantsev, M. A. Bloodgood, T. T. Salguero, A. A. Balandin, Nanoscale 2018, 10, 19749.

[33]    G. M. Sheldrick, Acta Crystallogr A Found Adv 2015, 71, 3.

[34]    G. M. Sheldrick, Acta Crystallogr C Struct Chem 2015, 71, 3.

[35]    O. V. Dolomanov, L. J. Bourhis, R. J. Gildea, J. A. K. Howard, H. Puschmann, J Appl Crystallogr 2009, 42, 339.

[36]    J. P. Perdew, K. Burke, M. Ernzerhof, *Phys Rev Lett* **1996**, 77, 3865.

[37]    G. Kresse, J. Furthmuller, *Phys Rev B Condens Matter* **1996**, 54, 11169.

The table of contents entry should be 50–60 words long and should be written in the present tense. The text should be different from the abstract text.

M. Fujioka*, M. Jeem, K. Sato, M. Tanaka, K. Morita T. Shibuya, K. Takahashi, S. Iwasaki, A. Miura, M. Nagao, S. Demura, H. Sakata, M. Ono, H. Kaiju, and J. Nishii

**Intercalation on transition metal trichalcogenides via a quasi-amorphous phase with 1D order**

The quasi-amorphous phase is a novel state of matter in which long-range order is lost while retaining 1D order. It is formed during the transition period from trigonal prismatic to octahedral phases via intercalation into transition metal trichalcogenides and has the potential to open a pathway to achieve high functionality such as electronic, ionic, and thermal transport properties.
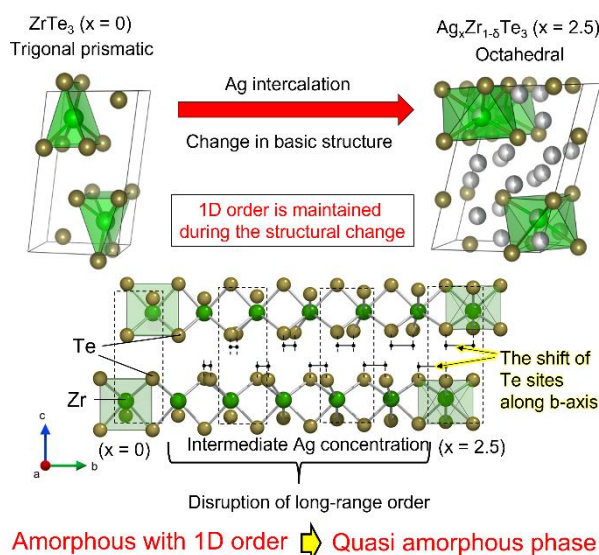
# Supporting Information

**Intercalation on transition metal trichalcogenides via a quasi-amorphous phase with 1D order**

*Masaya Fujioka\*, Melbert Jeem, Kento Sato, Masashi Tanaka, Kazuki Morita Taizo Shibuya, Kiyonori Takahashi, Suguru Iwasaki, Akira Miura, Masanori Nagao, Satoshi Demura, Hideaki Sakata, Madoka Ono, Hideo Kaiju, and Junji Nishii1*

OUTLINE

1. Detail of intercalation method

(a)

Needle shaped anode

$H_2 \rightarrow 2H^+ + 2e^-$

$H^+ + AgI \rightarrow Ag^+ + HI$

$Ag^+ + e^- + ZrTe_3$
$\rightarrow Ag_xZrTe_3$

$e^-$

$H^+$

$Ag^+$

Ag

ZrTe₃

Carbon Cathode

1 mm

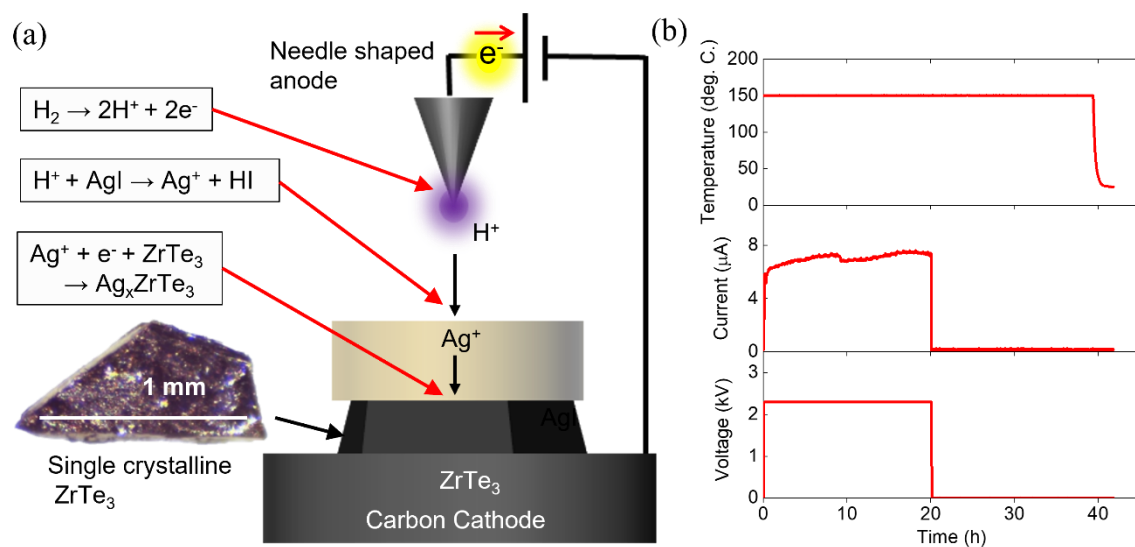Single crystalline ZrTe₃

(b)

**Figure S1.** (a) Schematic of proton-driven ion introduction (PDII) and the expected chemical formula in each indicated position. (b) Time dependence of voltage, current, and temperature. Applied voltage and total electricity are 2.3 kV and 0.4 C, respectively. Because the mass of a single crystal is ~2 mg, the introduced Ag ion can be estimated to be 1 equivalent in this case.
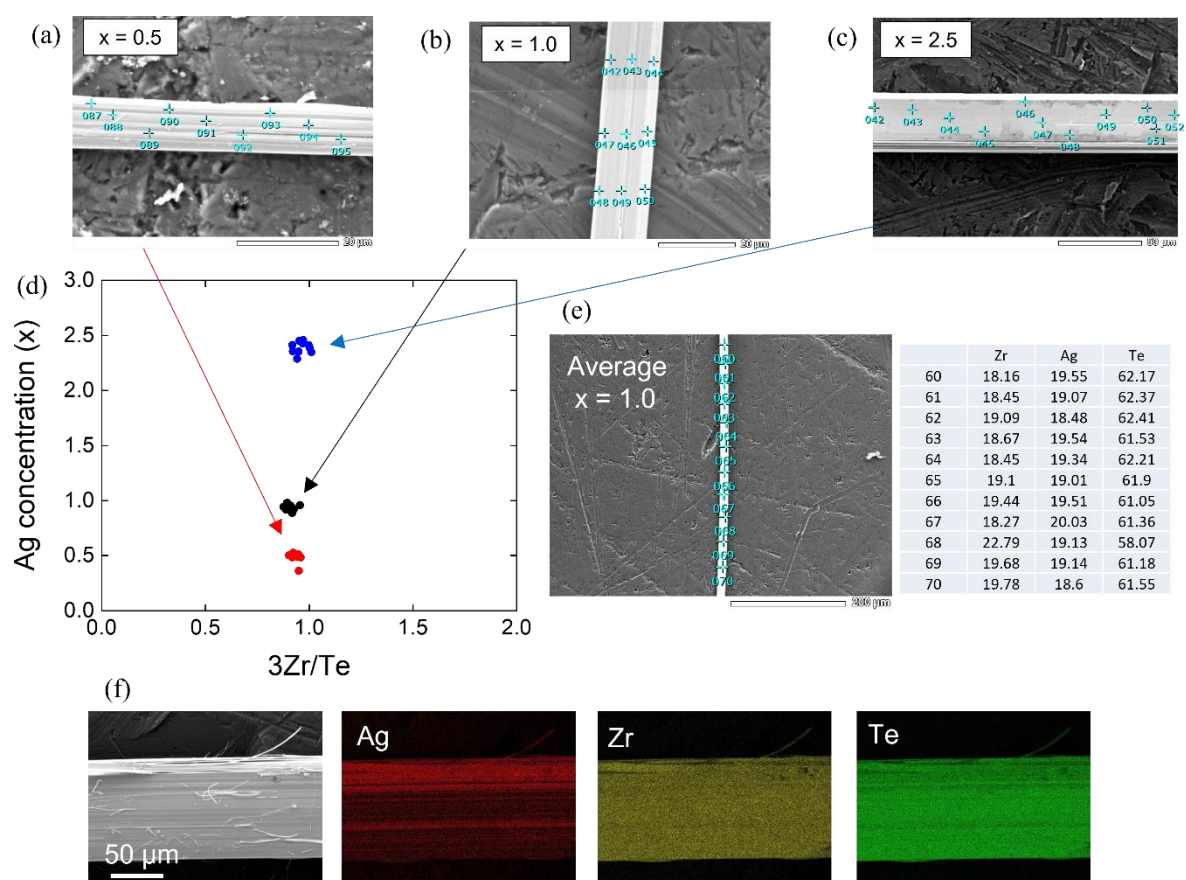
2. Microscale homogeneity observed from SEM-EDS analyses.



**Figure S2.** (a–c) SEM images for a finely peeled fiber with different Ag concentrations from the as-treated sample. (d) Summary of each quantitative point analysis of Ag concentrations (x) and the elemental ratio between Zr and Te normalized by Te. (e) The results of quantitative point analysis for the longitudinal direction of the fiber. (f) EDS mapping image of the lump of the sample with inhomogeneous Ag concentrations. The sample exhibits almost homogeneous Ag concentrations longitudinally: the *b*-axis. Because the obtained sample occasionally shows different Ag concentrations along the *a*-axis based on the size or position, whether the finely peeled fibers (a–c) have a homogeneous Ag distribution or not was carefully analyzed for structural and resistivity measurements.
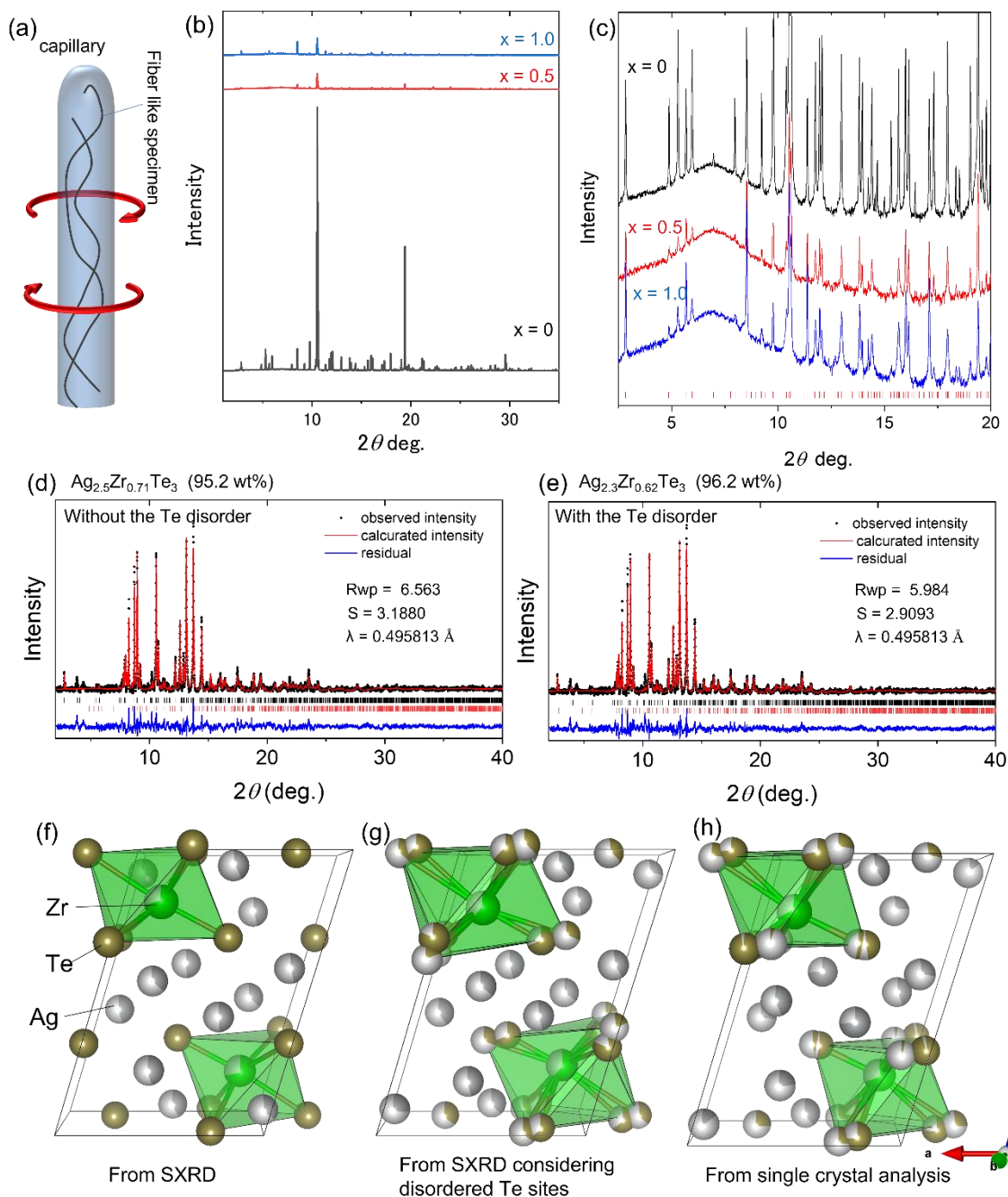
3. SXRD and single crystal XRD analysis.



**Figure S3.** (a) schematic configuration of fibers introduced capillary tube. (b) SXRD patterns for x = 0, 0.5, and 1.0 without normalization. (c) The same XRD patterns as (b) with the Y axis on a logarithmic scale. Red bars in the bottom correspond to the Bragg reflections of ZrTe$_3$. (d, e) Results of Rietveld refinements of SXRD pattern for x = 2.5 (d) with and (e) without considering the Te disorder. Black and red bars in the bottom correspond to the Bragg

reflections of $Ag_xZr_{1-\delta}Te_3$, and $ZrTe_3$, respectively. The proportions of $Ag_xZr_{1-\delta}Te_3$ in each analysis are 95.2 and 96.2wt%. (f) The crystal structure from (d) ($R_{wp}$: 6.563% and S: 3.1880). (g) The crystal structure from (e) ($R_{wp}$: 5.984% and S: 2.9093). (h) The crystal structure from single-crystal XRD analysis ($R$: 9.76%). **Table S1, S2** and **S3** summarize the structural parameters of (f), (g), and (h), respectively.

**Table S1.** Structural Information of Figure S3(f) obtained from Rietveld refinement without Te disorder ($Ag_{2.52}Zr_{0.712}Te_3$).

Space group *P 21/m*

$a$ = 7.6539(5) Å; $b$ = 4.1564(2) Å; $c$ = 10.804(7) Å; $\beta$ = 106.832(5)°

| site | Occupancy | *x* | *y* | *z* |
|------|-----------|-----|-----|-----|
| Zr | 0.712(11) | 0.1728(17) | 0.2500 | 0.1791(11) |
| Te1 | 1.0 | 0.4536(9) | 0.7500 | 0.6938(7) |
| Te2 | 1.0 | 0.7503(12) | 0.2500 | 0.0073(9) |
| Te3 | 1.0 | 1.0001(9) | 0.2500 | 0.6860(8) |
| Ag1 | 0.484(10) | 0.618(3) | 0.2500 | 0.590(2) |
| Ag2 | 0.367(7) | 0.756(3) | 0.7500 | 0.5390(16) |
| Ag3 | 0.456(10) | 0.356(2) | 0.2500 | 0.7841(16) |
| Ag4 | 0.412(11) | 0.468(3) | 0.2500 | 0.0507(19) |
| Ag5 | 0.351(11) | 1.025(3) | 0.7500 | 0.072(2) |
| Ag6 | 0.454(9) | 0.110(3) | 0.7500 | 0.5840(19) |

**Table S2.** Structural Information of Figure S3(g) obtained from Rietveld refinement with Te disorder ($Ag_{2.34}Zr_{0.616}Te_3$).

Space group *P 21/m*

$a = 7.6534(4)$ Å; $b = 4.1559$ (2) Å; $c = 10.8313$ (6) Å; $\beta = 106.838(4)°$

| site | Occupancy | $x$ | $y$ | $z$ |
|------|-----------|-----|-----|-----|
| Zr | 0.616(13) | 0.1813(18) | 0.25 | 0.2014(15) |
| Te1A | 0.685(14) | 0.4911(19) | 0.75 | 0.6832(12) |
| Te1B | 1-Te1A | 0.380(4) | 0.75 | 0.7022(17) |
| Te2A | 0.36(4) | 0.706(6) | 0.25 | 0.009(2) |
| Te2B | 1-Te2A | 0.784(3) | 0.25 | 0.9925(13) |
| Te3A | 0.81(2) | 0.9880(16) | 0.25 | 0.6992(13) |
| Te3B | 1-Te3A | 0.992(4) | 0.25 | 0.628(5) |
| Ag1 | 0.459(12) | 0.607(2) | 0.25 | 0.5857(19) |
| Ag2 | 0.358(6) | 0.716(3) | 0.75 | 0.520(2) |
| Ag3 | 0.463(12) | 0.361(2) | 0.25 | 0.8240(17) |
| Ag4 | 0.372(12) | 0.484(3) | 0.25 | 0.055(2) |
| Ag5 | 0.276(12) | 0.958(4) | 0.75 | 0.076(3) |
| Ag6 | 0.409(12) | 0.106(3) | 0.75 | 0.596(2) |

**Table S3.** Structural Information of Figure S3(h) obtained from single-crystal XRD analysis ($Ag_{2.23}Zr_{0.683}Te_3$).

Space group *P 21/m*

$a = 7.6446(11)$ Å; $b = 4.1496(4)$ Å; $c = 10.8162(17)$ Å; $\beta = 107.039(17)°$

| site | Occupancy | $x$ | $y$ | $z$ |
|------|-----------|-----|-----|-----|
| Zr | 0. 683(18) | 0.1661(6) | 0.25 | 0.1951(5) |
| Te1A | 0. 53(9) | 0.486(7) | 0.75 | 0.6921(15) |
| Te1B | 1-Te1A | 0.4504(17) | 0.75 | 0.6882(19) |
| Te2A | 0. 74(4) | 0.7932(6) | 0.25 | 0.9905(12) |
| Te2B | 1-Te2A | 0.711(11) | 0.25 | 0.0085(14) |
| Te3A | 0. 961(7) | 0.9902(4) | 0.25 | 0.6835(3) |
| Te3B | 1-Te3A | 0.881(11) | 0.25 | 0.699(7) |
| Ag1 | 0. 743(15) | 0.6132(5) | 0.25 | 0.5829(4) |
| Ag2 | 0. 442(16) | 0.7917(12) | 0.75 | 0.4926(9) |
| Ag3 | 0. 229(16) | 0.348(3) | 0.25 | 0.8075(13) |
| Ag4 | 0. 392(15) | 0.4815(13) | 0.25 | 0.0513(12) |
| Ag5 | 0. 146(15) | 0.961(5) | 0.75 | 0.053(2) |
| Ag6 | 0. 273(15) | 0.149(2) | 0.75 | 0.5859(12) |

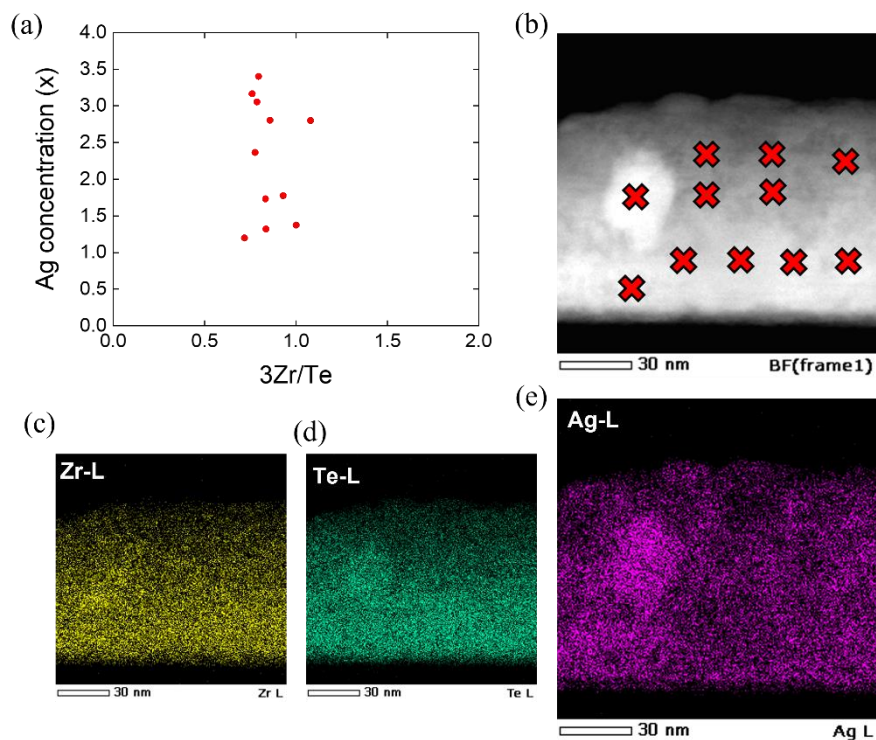4. Nanoscale inhomogeneity observed from STEM-EDS analyses



**Figure S4.** (a) Summary of each quantitative point analysis of the Ag concentration (x) and the elemental ratio between Zr and Te normalized by Te from STEM–EDS measurements for the sample in the quasi-amorphous phase. (b) Nanoscale region in the quasi-amorphous phase with red crosses indicates the analyzed points of (a). (c-e) Mapping images of (c) Zr, (d) Te, and (e) Ag.
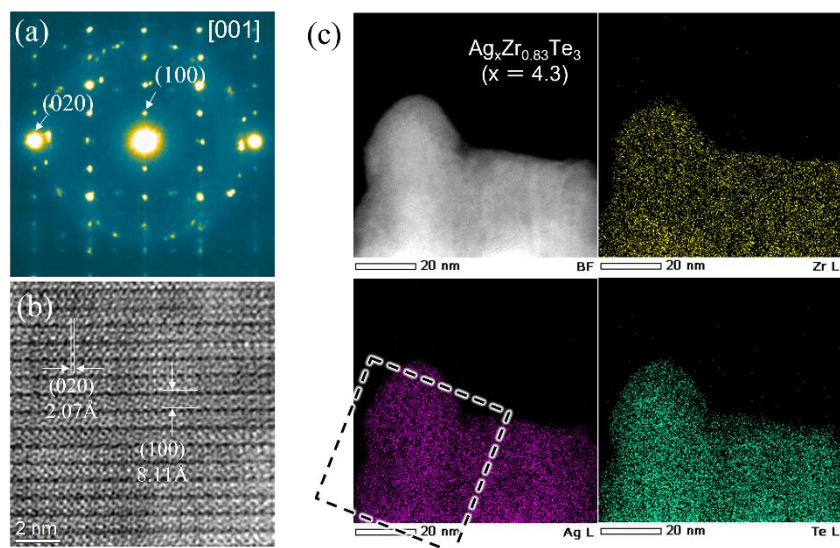
**Figure S5.** (a) [001] SAED pattern in the quasi-amorphous region and its (b) HRTEM image. (c) STEM–EDS mapping result for a sample with extremely high Ag concentrations. Dotted black square represents the analyzed region of (a).
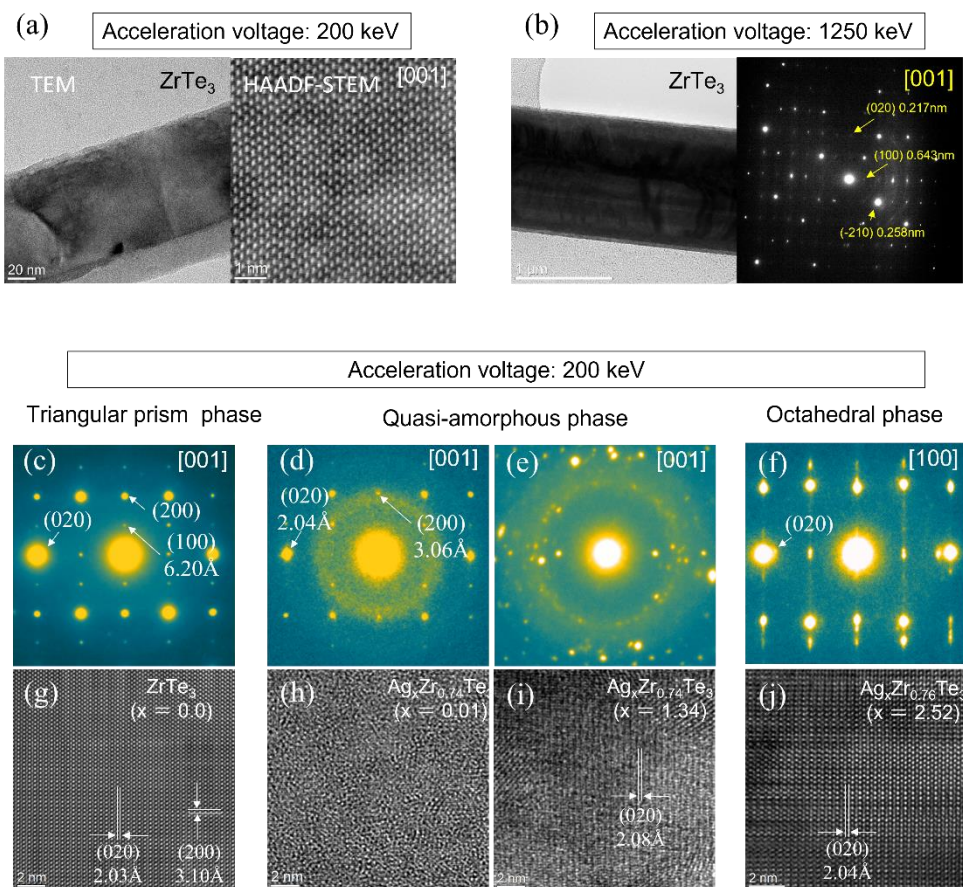
5. The effect of electron beam irradiation



**Figure S6.** (a) Typical fiber-like ZrTe₃ TEM sample and its atomic resolution HAADF-STEM image. (b) ZrTe₃ sample surface subjected to TEM at 1250 keV and its [001] SAED pattern. (c–f) SAED for the sample with different Ag concentrations at 200 keV. (g–j) HRTEM images corresponding to each sample in (c–f), respectively.

The $a$ lattice constant of the parent compound ($ZrTe_3$) is estimated to be 5.89 Å from SXRD measurements. However, the detected $d$-values of the (100) plane are 6.20 Å at 80 and 200 keV (**Figure 2(a)** and **S6(c)**, respectively) and 6.43 Å at 1250 keV (**Figure S6(b)**) from SAED measurements. Therefore, electron irradiation with high accelerating voltages expands the $a$ lattice constant in **Figure S6(b)** and **Figure S6(c)**. This expansion is also observed after Ag intercalation: 7.65Å from SXRD measurements increased to 7.99 Å from SAED measurements at 80 keV. An absolute explanation for this phenomenon cannot be proposed

currently.

Electron beam irradiation damages the samples. At 200 keV, $Ag_xZr_{1-\delta}Te_3$ is amorphized, and at 1250 keV, $ZrTe_3$ immediately undergoes fine crystallization. Although, at 200 keV, the deterioration of the structure owing to Ag diffusion is evident based on observations, at 80 keV, no visible sample deterioration is confirmed, even from long-term measurements. In this study, all diffraction and high-resolution images in **Figure 2** are obtained at an accelerating voltage of 80 keV.
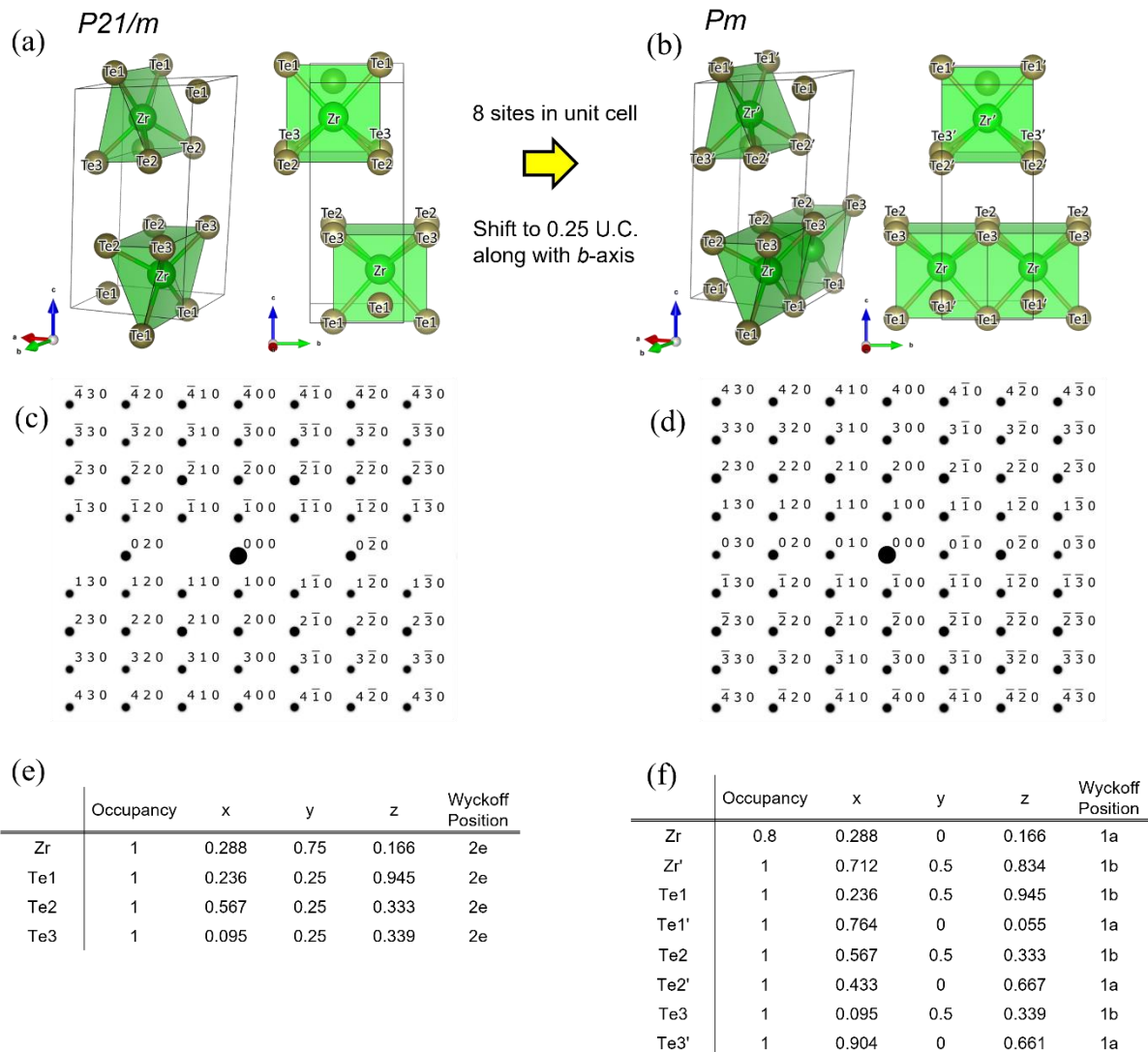


**Figure S7.** (a, b), Crystal structures of $ZrTe_3$ with space groups (a) $P2_1/m$ and (b) Pm. (c–f), Simulated diffraction spots of (c) $P2_1/m$ and (d) Pm from the structural Information of (e) and

(e)

|  | Occupancy | x | y | z | Wyckoff Position |
|---|---|---|---|---|---|
| Zr | 1 | 0.288 | 0.75 | 0.166 | 2e |
| Te1 | 1 | 0.236 | 0.25 | 0.945 | 2e |
| Te2 | 1 | 0.567 | 0.25 | 0.333 | 2e |
| Te3 | 1 | 0.095 | 0.25 | 0.339 | 2e |

(f)

|  | Occupancy | x | y | z | Wyckoff Position |
|---|---|---|---|---|---|
| Zr | 0.8 | 0.288 | 0 | 0.166 | 1a |
| Zr' | 1 | 0.712 | 0.5 | 0.834 | 1b |
| Te1 | 1 | 0.236 | 0.5 | 0.945 | 1b |
| Te1' | 1 | 0.764 | 0 | 0.055 | 1a |
| Te2 | 1 | 0.567 | 0.5 | 0.333 | 1b |
| Te2' | 1 | 0.433 | 0 | 0.667 | 1a |
| Te3 | 1 | 0.095 | 0.5 | 0.339 | 1b |
| Te3' | 1 | 0.904 | 0 | 0.661 | 1a |

(f), respectively.

The space group of $ZrTe_3$ is $P2_1/m$. However, the observed [001] SAED pattern did not indicate $P2_1/m$. The (010) plane reflections are observed despite the extinction rules on $P2_1/m$ (**Figure 2(a)** and **S6(c)**). The same SAED pattern is also observed in the previous research [32b]. Each element of $ZrTe_3$ belongs to the 2e site of $P2_1/m$. If the electron beam distorts the structure or forms a defect randomly and the two atoms in the site can be distinguished separately, the symmetry is reduced to Pm and each atom is recognized to be in the 1a and 1b sites of Pm. For instance, when introducing a defect into a Zr site, as shown in **Figure S7(f)**, the diffraction spot of the (010) plane is detected. On the other hand, single-crystal XRD analysis showed that $ZrTe_3$ belongs to $P2_1/m$. Although an acceleration voltage of 80 keV reduces the beam damage significantly, the influence of electron beams on to sample is controversial.

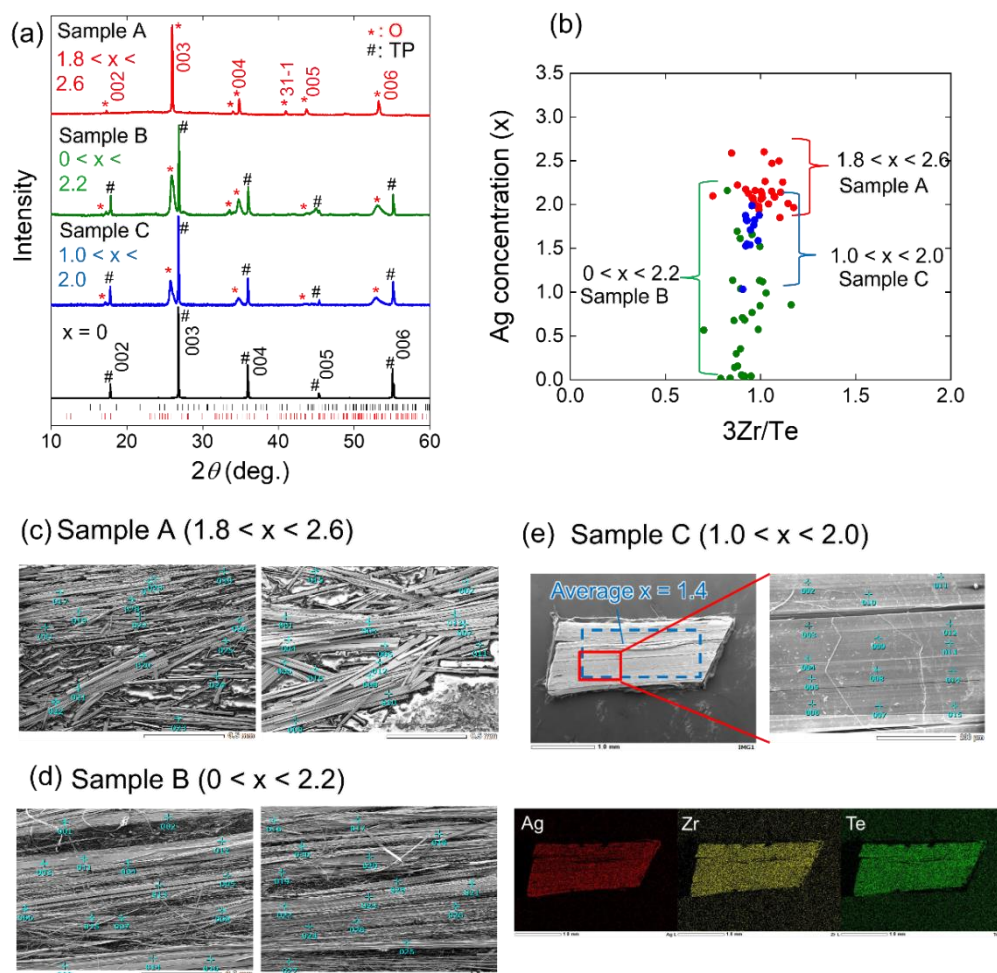6.   Structural transition via quasi-amorphous phase.



**Figure S8.** (a) XRD patterns for four samples with different Ag concentrations and distribution. Samples A and B were prepared by cleaving using a Scotti tape multiple times. Flexible fibrous bodies are fixed using adhesive tape with a *c*-axis orientation. Sample C maintained bulk shape after Ag introduction by stopping Ag intercalation before degrading into fibers. (b) The summary of each quantitative point analysis of Ag concentrations (*x*) and the elemental ratio between Zr and Te normalized by Te. Ag concentrations are estimated to be $1.8 < x < 2.6$, $0 < x < 2.2$, and $1.0 < x < 2.0$ for Samples A, B, and C, respectively. (c, d) SEM-EDS measurements for samples (c) A and (d) B. Green crosses indicate the position of quantitative point analysis. (e) SEM-EDS measurements for quantitative analysis and mapping images of sample C. Area analysis was conducted in the region enclosed by blue dashed line.

41
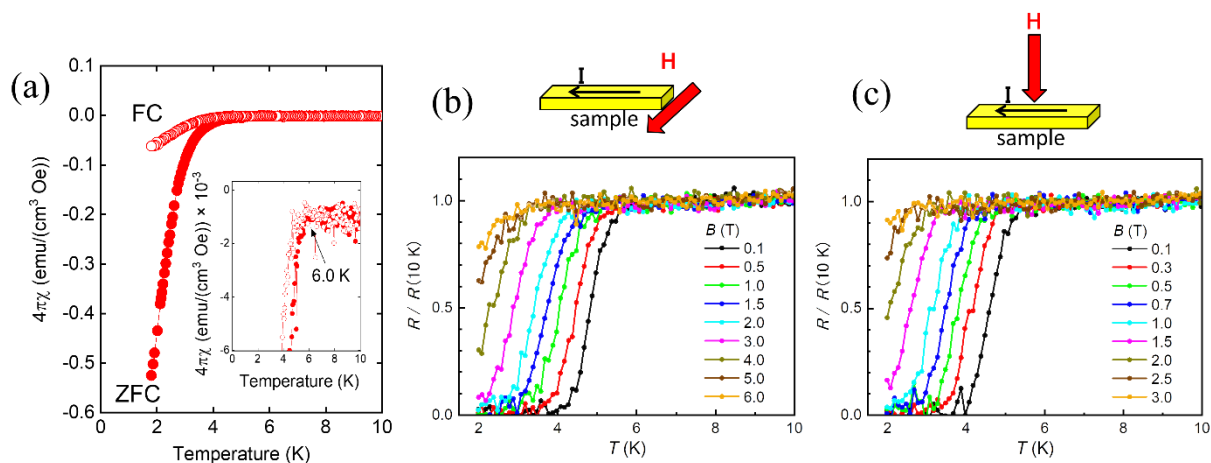
## 7. Superconducting properties



**Figure S9.** (a) The temperature dependence of magnetic susceptibility under 10 Oe. (b, c) The temperature dependence of normalized resistivity under magnetic field parallel to the (b) *a*-axis and (c) *c*-axis. Magnetization measurements are performed using the as-prepared large lump comprising many fibers with varying Ag concentrations. Most of the fibers are not optimally doped with x = 0.5. Therefore, the magnetic susceptibility curve starts dropping at ~6 K, but most regions change to a superconducting state at ~4 K.

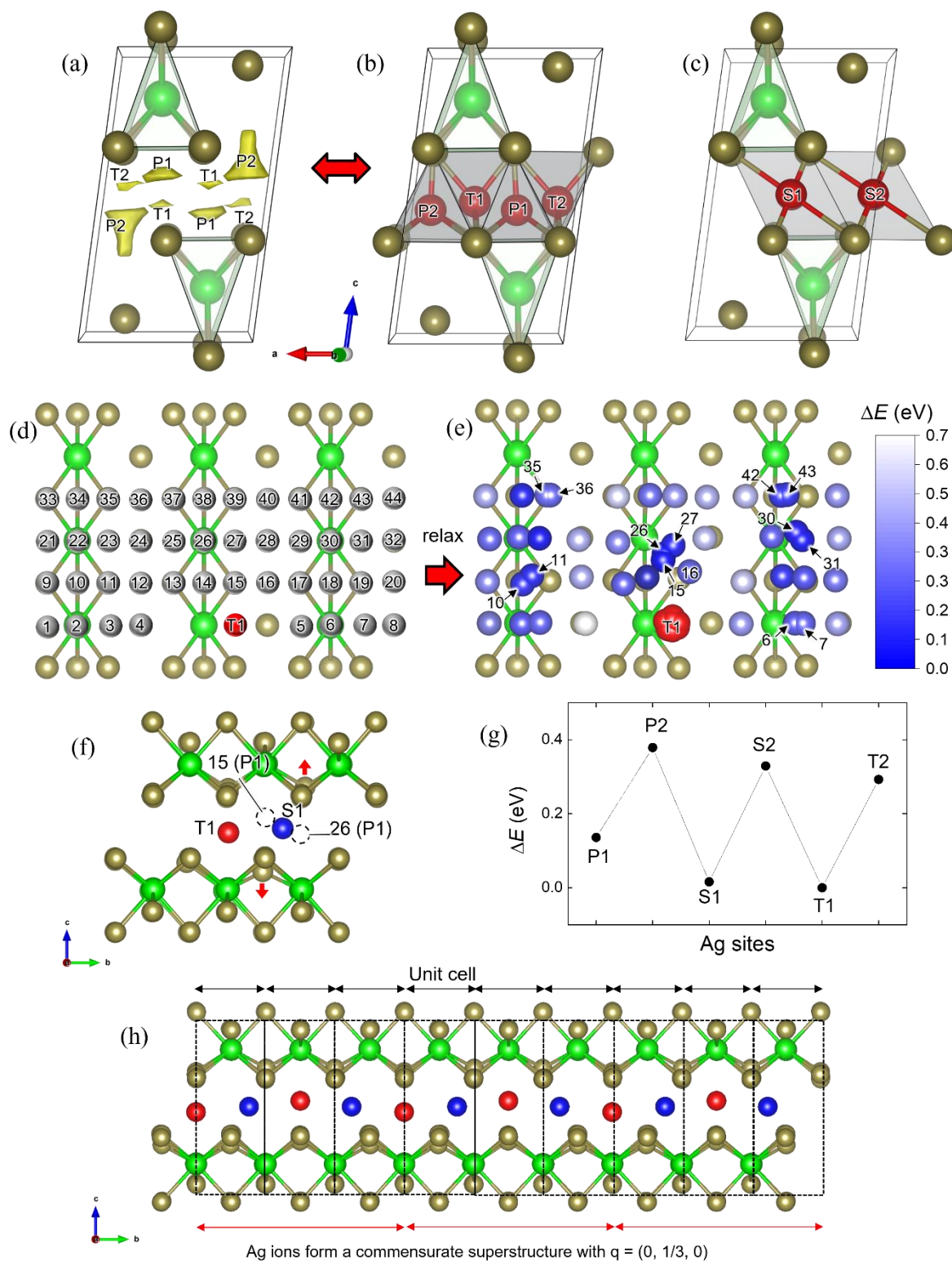8. Stable sites for Ag ions at the initial stage of intercalation.



**Figure S10.** (a) Energy landscape for an Ag ion in ZrTe$_3$. Spaces enclosed by yellow isosurfaces represent stable sites for Ag ions. The isosurface level is 173 meV/atom. These energetic local minimum for Ag ions can be found by exploring energy landscapes, namely,

43

by calculating the total energies of the unit cell ($Zr_2Te_6$) with an Ag ion at different positions. The position of the Ag ion varies over the entire unit cell. The pitch of the variation is approximately 0.3 Å for each axis, producing about 10,000 configurations. (b) Four stable sites in $ZrTe_3$. Tetrahedral (T1 and T2) and pyramid (P1 and P2) spaces are formed by Te atoms, corresponding to an energetic local minimum, as shown in a. (c) Other candidates for Ag stable sites. The ionic relaxation suggested the square (S1) spaces as additional stable Ag sites. S2 site has the same Te coordination environment as S1. (d) Summarized initial configuration of $Ag_2Zr_{18}Te_{54}$ supercells ($3 \times 3 \times 1$). One Ag ion is placed at the T1 site, as indicated by the red atom. Second Ag ion is placed at P1, P2, T1, and T2 sites each, numbered from 1 to 44. Forty-four configurations with different positions of the second Ag ion are depicted in the same Figure. (e) Summarized configuration after relaxation. The difference in total energy ($\Delta E$) between the most stable configuration, where the second Ag ion is placed at position 15, and each other configuration is shown by the color of the second Ag ion. The darker the blue color, the more stable the configuration. (f) Shifting of Ag ions from position 15 and position 26. The circle indicated by the dotted lines shows the initial position of the second Ag ion. It moves to the intermediate position between 15 and 26, at the same time, nearby Te ions spread up and down, forming a new stable space for Ag ions. This stable site is located at the center of the square formed by Te atoms and is denoted as the S1 site. Thus, the additional stable state can be found when the second Ag ions are placed near the first Ag ion in the same fiber. (g) Most stable site among 6 candidates: P1, P2, T1, T2, S1, and S2. The total energies of $AgZr_{18}Te_{54}$ supercell ($3 \times 3 \times 1$) with different Ag positions are compared. T1 site is the most stable among them. The three most stable sites (T1, S1, P1) are mentioned in the main text as (T, S, and P), respectively. (h) Suggested commensurate structure considering the newly formed S sites.

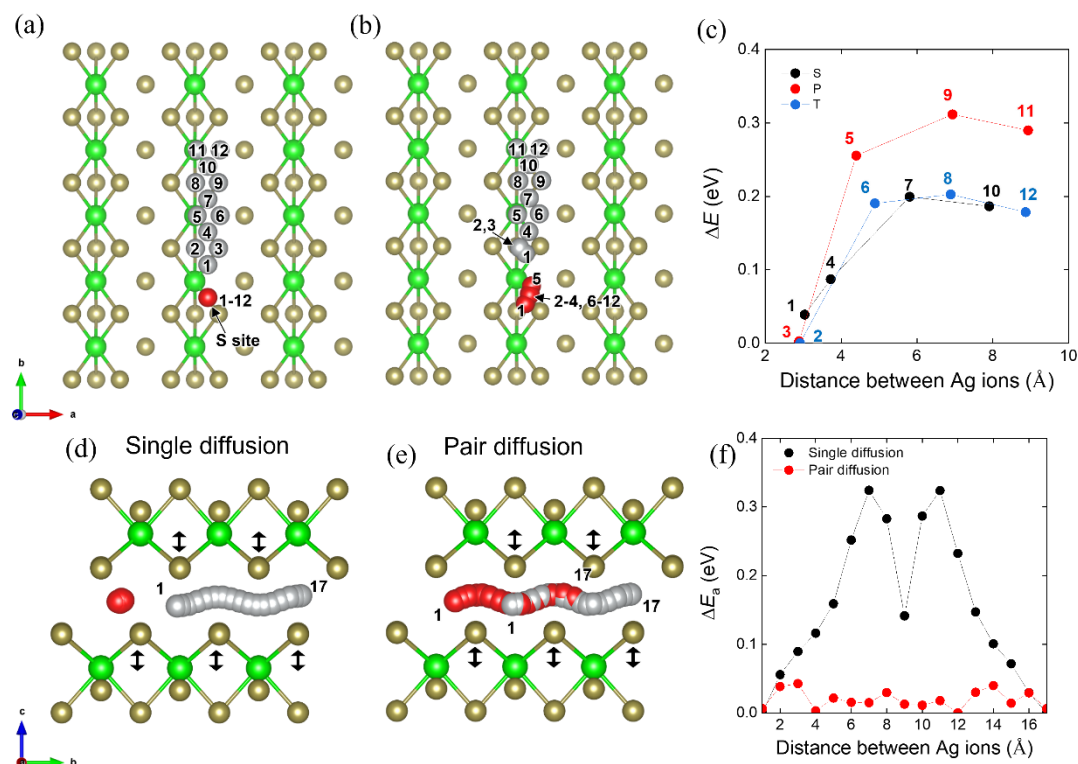9. The local attraction between guest ions and activation energy.



**Figure S11.** (a) Summarized initial configuration of $Ag_2Zr_{30}Te_{90}$ supercells ($3 \times 5 \times 1$). One Ag ion is placed at the S site, as indicated by the red atom. Second Ag ion is placed at S, P, and T sites each, denoted by 1, 4, 7, and 10 for S, 3, 5, 9, 11 for P, and 2, 6, 8, and 12 for T. Twelve configurations with different positions of the second Ag ion are depicted in the same Figure (a). (b) Summarized configuration of $Ag_2Zr_{30}Te_{90}$ supercells ($3 \times 5 \times 1$) after ionic relaxation. Each configuration after ionic relaxation is combined in (b). (c) Local attraction as a function of the distance between Ag ions. (d, e) Ag ion paths with the interaction between Ag ions for the (d) single diffusion and (e) pair diffusion along with the *b*-axis using NEB method. (f) Activation energy ($\Delta E_a$) for single (d) and pair (e) diffusions of Ag ions.
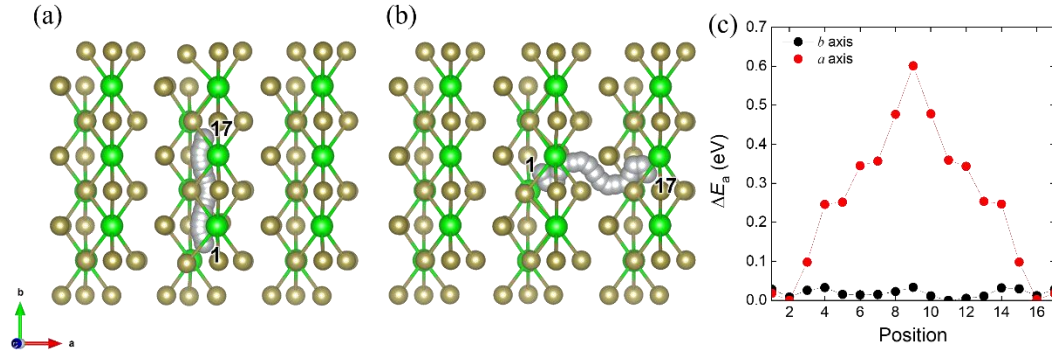
**Figure S12.** (a, b) Ag ion paths along (a) *b*- and (b) *a*-axes. c, Activation energy ($\Delta E_a$) along *b*- and *a*-axes. Ag ion diffuses between S sites.



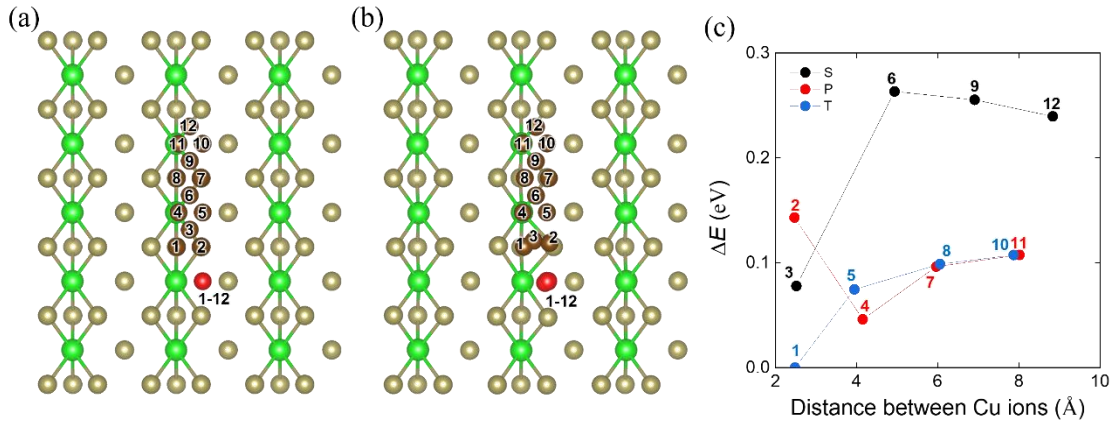**Figure S13.** (a) Summarized initial configuration of $Cu_2Zr_{30}Te_{90}$ supercells ($3 \times 5 \times 1$). One Cu ion is placed at the T site, as indicated by the red atom. Second Cu ion is placed at S, P, and T sites each, denoted by 3, 6, 9, and 12 for S, 2, 4, 7, 11 for P, and 1, 5, 8, and 10 for T, as is the case with the Ag ion (**Figure 4b**). Twelve configurations with different positions of the second Cu ion are depicted in the same Figure (a). (b) Summarized configuration of $Cu_2Zr_{30}Te_{90}$ supercells ($3 \times 5 \times 1$) after ionic relaxation. Each configuration after ionic relaxation is combined in (b). (c) Local attraction as a function of the distance between Cu ions.
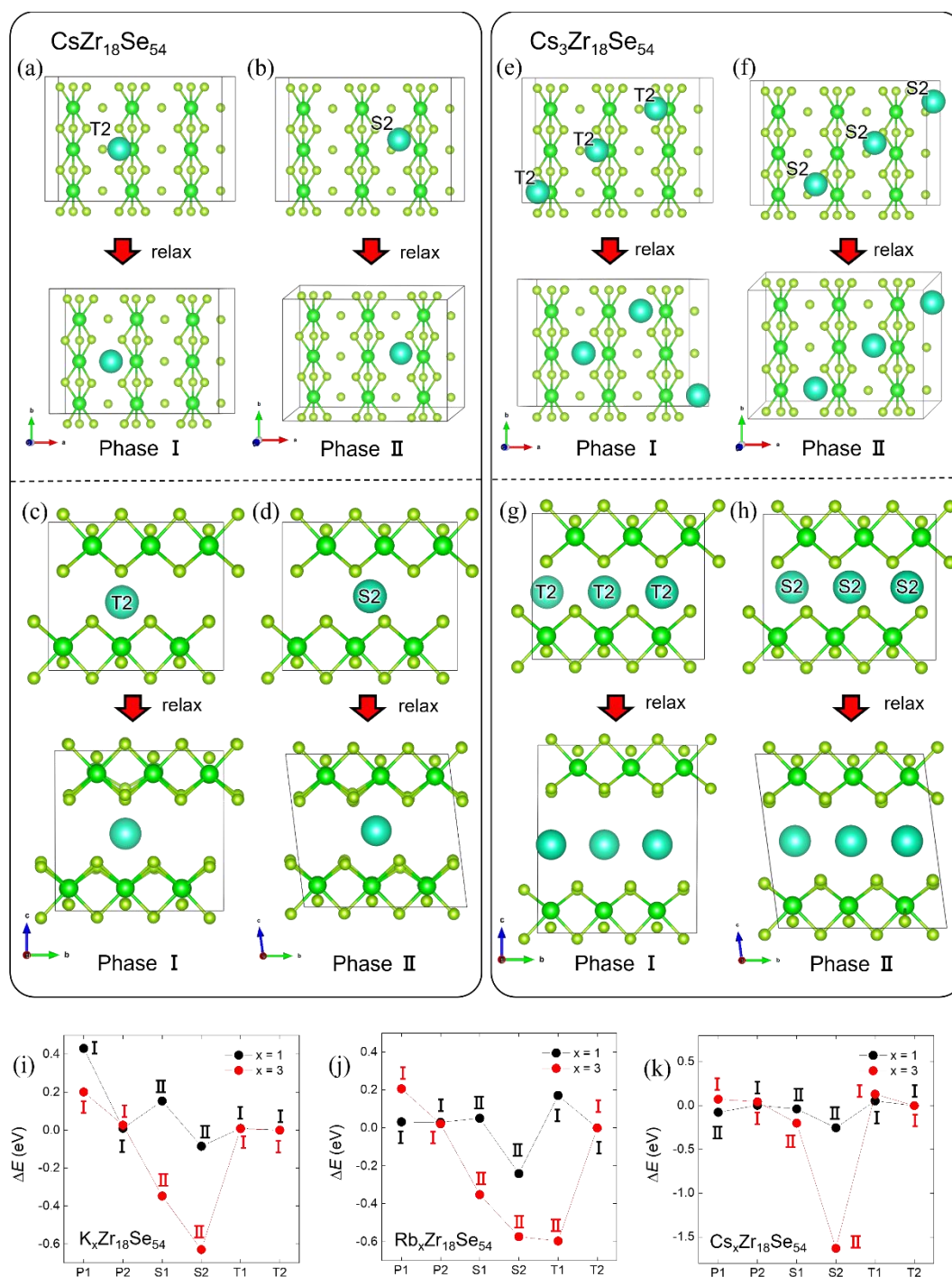
10. The case of ZrSe$_3$ with the c-lattice extension.



**Figure S14.** (a, b) Configurations of CsZr$_{18}$Se$_{54}$ on the projection of the *ab* plane before and after relaxation. A Cs ion is placed at (a) T2 and (b) S2 sites. (c, d) Configurations of CsZr$_{18}$Se$_{54}$ on the projection of the *bc* plane before and after relaxation. A Cs ion is placed at (c) T2 and (d) S2 sites. (e, f) Configurations of Cs$_3$Zr$_{18}$Se$_{54}$ on the projection of the *ab* plane

before and after relaxation. Three Cs ions are placed at (e) T2 and (f) S2 sites. (g, h)

Configurations of $Cs_3Zr_{18}Se_{54}$ on the projection of the $bc$ plane before and after relaxation.

Three Cs ions are placed at (g) T2 and (h) S2 sites. When Cs ions are placed at T2 site, the $c$

lattice parameter is simply expanded after relaxation. When Cs ions are placed at S2 site, the

α angle is greatly distorted after relaxation. The former structure after relaxation is denoted as

Phase I, and the later structure after relaxation is denoted as Phase II. (i–k) Phase stability

between the Phase I and II for (i) $K_xZr_{18}Se_{54}$, (j) $Rb_xZr_{18}Se_{54}$, and (k) $Cs_xZr_{18}Se_{54}$, when guest

ions are placed at the P1, P2, T1, T2, S1 and S2 site. Phase II tends to be stable in all

compounds when the guest ions are placed at S1 or S2 and the guest ion concentration
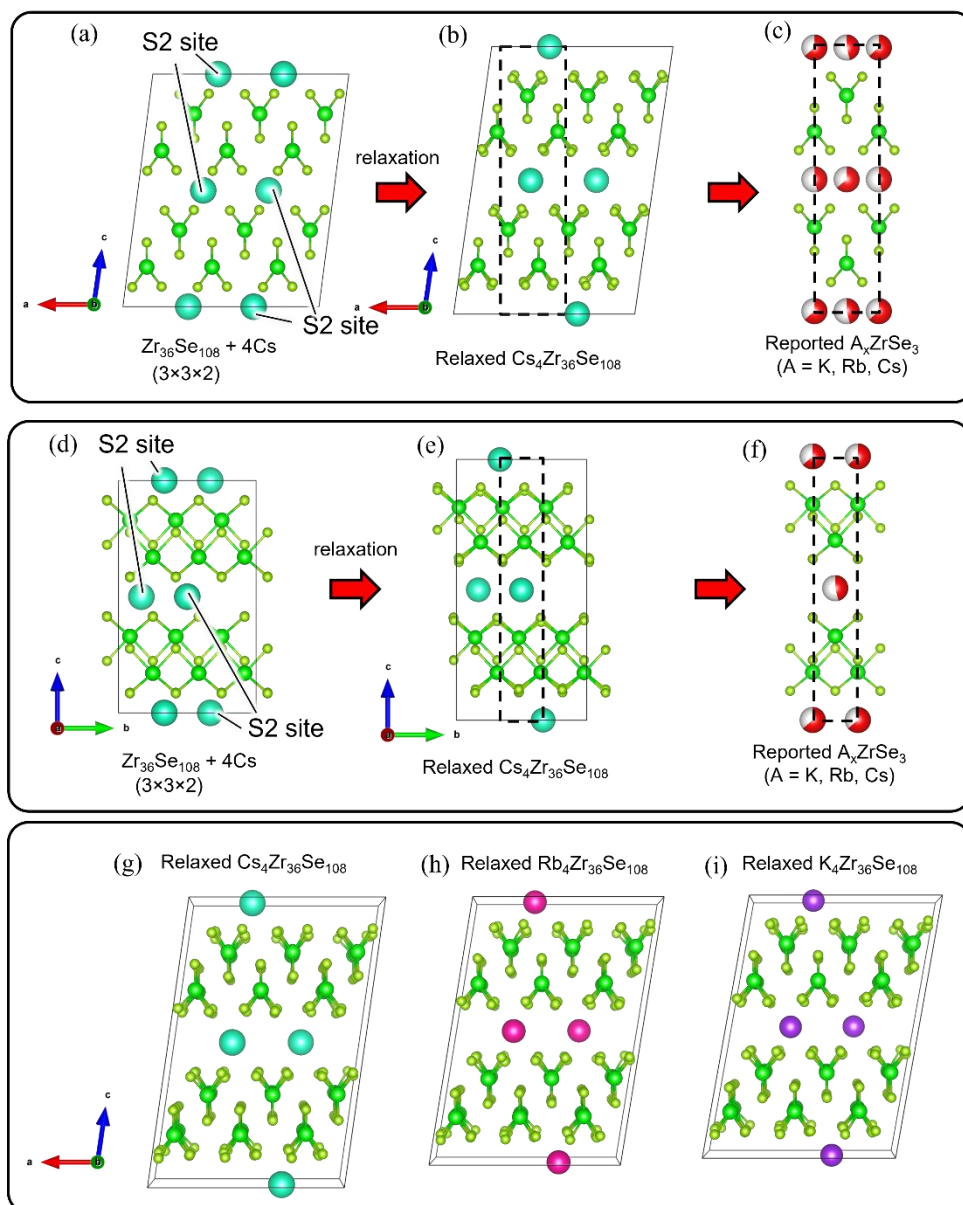
increases.

**Figure S15.** (a) Initial configuration of a $Cs_4Zr_{32}Se_{108}$ supercell ($3 \times 3 \times 2$) based on the projections of the *ca* plane. (b) Relaxed structure of (a). (c) Reported structure of $A_xZrSe_3$ ($A$ = K, Rb, and Cs). (d) Initial configuration of the $Cs_4Zr_{32}Se_{108}$ supercell ($3 \times 3 \times 2$) based on the projections of the *bc* plane. (e), Relaxed structure of (d). (f) Reported structure of $A_xZrSe_3$ ($A$ = K, Rb, and Cs). When the guest ions are placed at S1 and S2 sites, the structure changes to Phase II as a more stable state (**Figure S14**). This phase shows a similar crystal structure of $A_xZrSe_3$ via solid-state reaction. The DFT calculations can reproduce the reported $A_xZrSe_3$ by guest ion intercalation to $ZrSe_3$.

11. Interaction between guests according to the combination of the hosts and guests.
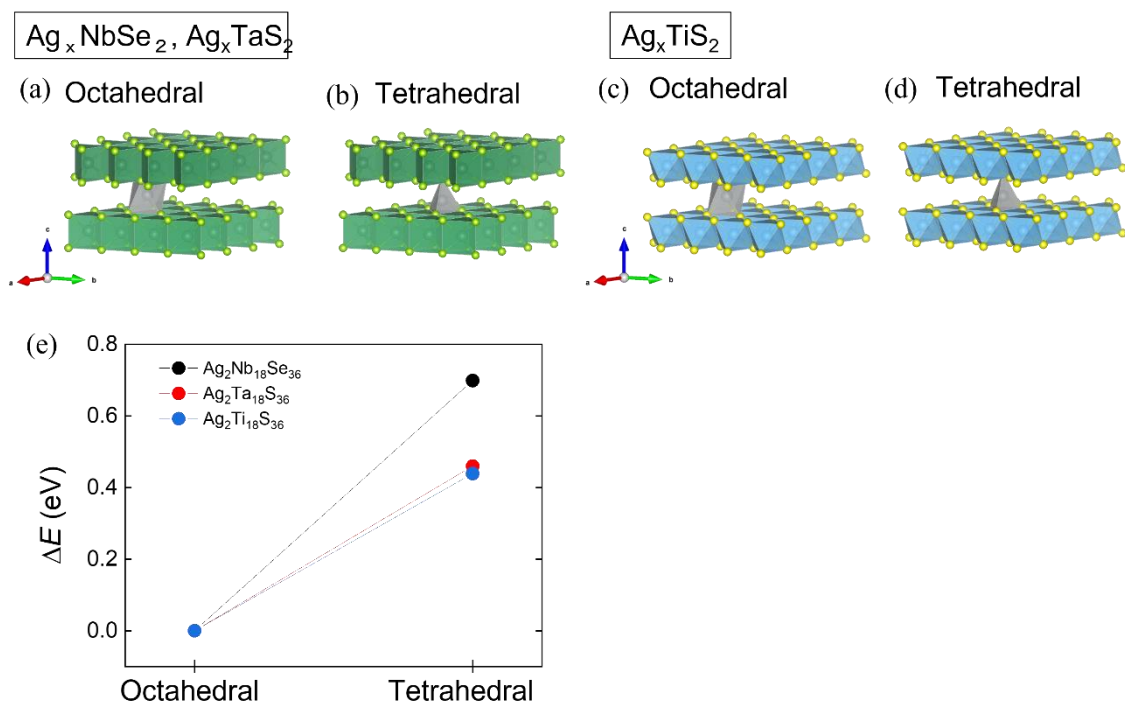
$Ag_xNbSe_2$, $Ag_xTaS_2$

(a) Octahedral    (b) Tetrahedral

$Ag_xTiS_2$

(c) Octahedral    (d) Tetrahedral



(e)



**Figure S16.** (a, b) Configurations with Ag ions located at the (a) octahedral site and (b) tetrahedral site for $Ag_xNbSe_2$ and $Ag_xTaS_2$. (c, d) Configurations with Ag ions located at the (c) octahedral site and (d) tetrahedral site for $Ag_xTiS_2$. (e), Difference in the total energy ($\Delta E$) between $AgM_{18}X_{36}$ ($M$ = Nb and Ta; $X$ = Se and S) with Ag ion placed at octahedral and tetrahedral sites.
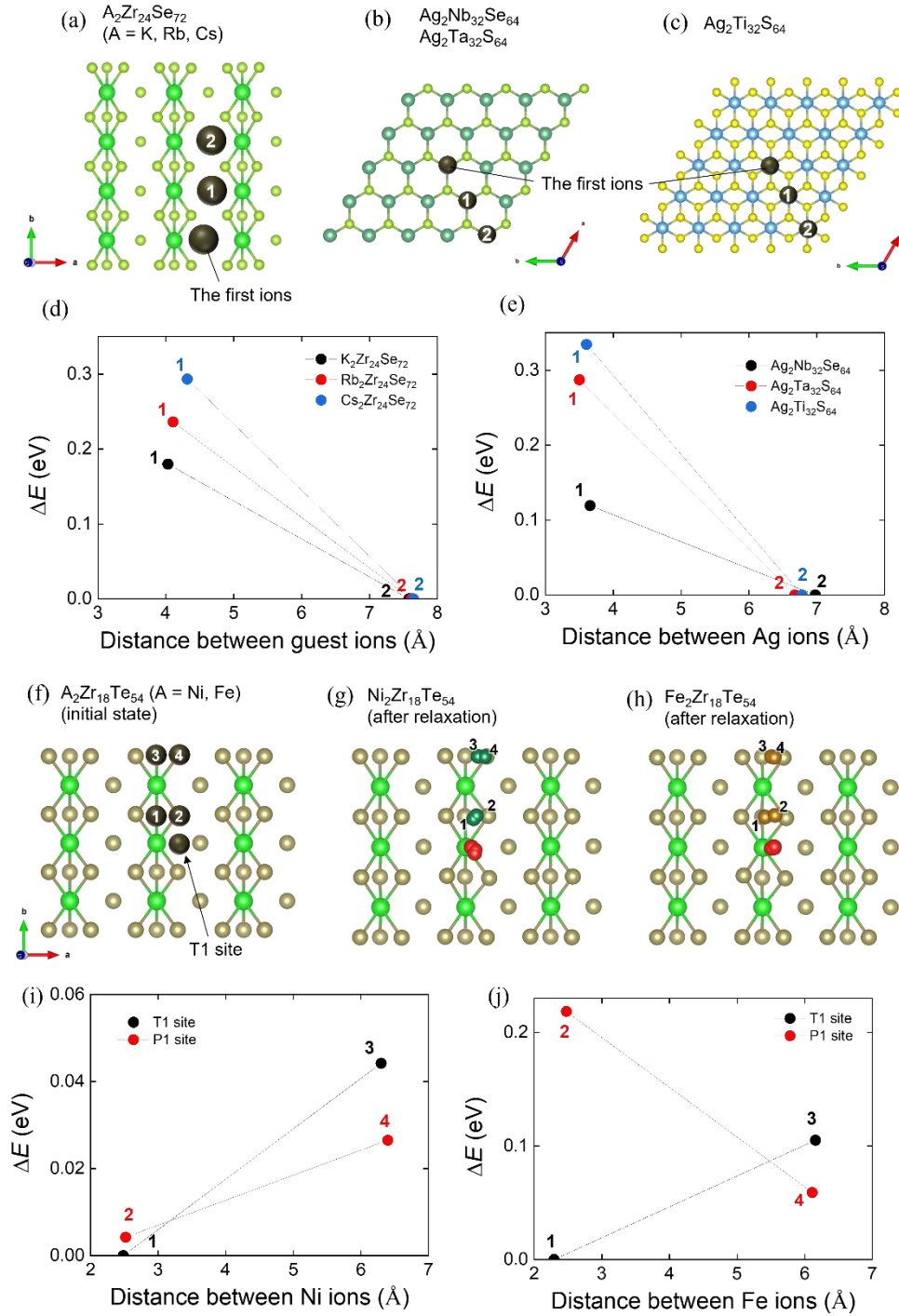
**Figure S17.** (a) Summarized configuration of supercells ($3 \times 4 \times 1$) of $A_2Zr_{24}Se_{72}$ ($A$ = K, Rb, and Cs). (b) Summarized configuration of supercells ($4 \times 4 \times 1$) of $Ag_2Nb_{32}Se_{64}$ and $Ag_2Ta_{32}S_{64}$. (c) Summarized configuration of supercells ($4 \times 4 \times 2$) of $Ag_2Ti_{32}S_{64}$. One guest ion is placed at a described position in (a-c). Second guest ion is denoted by 1, and 2 in (a-c). Two configurations with different positions of the second ions are depicted in the same Figure (a-c). (d) Difference in the total energy ($\Delta E$) between $A_2Zr_{24}Se_{72}$ ($A$ = K, Rb, and Cs) with the

second $A$ ion located at positions 1 and 2. (e) $\Delta E$ between $AgM_{18}X_{36}$ ($M$ = Nb and Ta; $X$ = Se and S) with the second Ag ion located at positions 1 and 2. (f) Summarized initial configuration of supercells (3 × 3 × 1) of $A_2Zr_{18}Te_{54}$ ($A$ = Ni, and Fe). (g) Summarized configuration of supercells (3 × 3 × 1) of $Ni_2Zr_{18}Te_{54}$ after relaxation. (h) Summarized configuration of supercells (3 × 3 × 1) of $Fe_2Zr_{18}Te_{54}$ after relaxation. One guest ion is placed at the site T1 in (f-h). Second guest ion is denoted by 1, 2, 3, and 4 in (f-h). Four configurations with different positions of the second ions are depicted in the same Figure (f-h). (i, j) $\Delta E$ of $A_2Zr_{18}Te_{54}$ ($A$ = Ni, and Fe) between the most stable configuration and each other configuration. Note that both ionic position and lattice parameter were relaxed in all configurations in **Figure S17**. In particular, there is no experimental information on the lattice constant of Ni and Fe intercalated $ZrTe_3$.

**Table S4.** Lattice parameters of $Ag_xZr_{18}Te_{54}$ (x = 1, 2) and $A_2Zr_{30}Te_{90}$ (A = Ag, Cu,)

| $Ag_xZr_{18}Te_{54}$ | $a$ (Å) | $b$ (Å) | $c$ (Å) | $\alpha$ (°) | $\beta$ (°) | $\gamma$ (°) |
|---|---|---|---|---|---|---|
| (x = 1) | 5.9339 | 3.9315 | 10.120 | 90 | 98.128 | 90 |
| (x = 2) | 5.9730 | 3.9366 | 10.135 | 90 | 98.326 | 90 |
| $A_2Zr_{30}Te_{90}$ | $a$ (Å) | $b$ (Å) | $c$ (Å) | $\alpha$ (°) | $\beta$ (°) | $\gamma$ (°) |
| (A = Ag) | 5.9417 | 3.9325 | 10.123 | 90 | 98.167 | 90 |
| (A = Cu) | 5.9400 | 3.9310 | 10.105 | 90 | 97.422 | 90 |

The lattice parameters of $Ag_xZr_{18}Te_{54}$ (x = 1, 2) and $A_2Zr_{30}Te_{90}$ (A = Ag, Cu,) are estimated

based on the linear relation between the guest ion concentration and experimentally obtained

crystal structures: $Ag_{2.5}ZrTe_3$ (**Table S1**), $Cu_2ZrTe_3$,[23] and $ZrTe_3$ parent compound.[9]